Predicting the lithospheric stress field and plate motions by joint modeling of lithosphere and mantle dynamics

A. Ghosh,[1,2] W. E. Holt,[1] and L. Wen[1,3]

Received 11 June 2012; revised 1 November 2012; accepted 13 November 2012; published 30 January 2013.

[1] The way in which basal tractions, associated with mantle convection, couples with the lithosphere is a fundamental problem in geodynamics. A successful lithosphere-mantle coupling model for the Earth will satisfy observations of plate motions, intraplate stresses, and the plate boundary zone deformation. We solve the depth integrated three-dimensional force balance equations in a global finite element model that takes into account effects of both topography and shallow lithosphere structure as well as tractions originating from deeper mantle convection. The contribution from topography and lithosphere structure is estimated by calculating gravitational potential energy differences. The basal tractions are derived from a fully dynamic flow model with both radial and lateral viscosity variations. We simultaneously fit stresses and plate motions in order to delineate a best-fit lithosphere-mantle coupling model. We use both the World Stress Map and the Global Strain Rate Model to constrain the models. We find that a strongly coupled model with a stiff lithosphere and 3–4 orders of lateral viscosity variations in the lithosphere are best able to match the observational constraints. Our predicted deviatoric stresses, which are dominated by contribution from mantle tractions, range between 20–70 MPa. The best-fitting coupled models predict strain rates that are consistent with observations. That is, the intraplate areas are nearly rigid whereas plate boundaries and some other continental deformation zones display high strain rates. Comparison of mantle tractions and surface velocities indicate that in most areas tractions are driving, although in a few regions, including western North America, tractions are resistive.

Citation: Ghosh, A., W. E. Holt, and L. Wen (2013), Predicting the lithospheric stress field and plate motions by joint modeling of lithosphere and mantle dynamics, *J. Geophys. Res. Solid Earth*, *118*, 346–368, doi:10.1029/2012JB009516.

1. Introduction

[2] The plate-mantle coupling problem has been one of the central problems in present-day geodynamics. It refers to the way deeper, density buoyancy-driven mantle tractions affect lithospheric deformation. This coupling problem has implications on the questions of what drives the Earth's tectonic plates, what role does mantle convection play, and what is the nature of coupling between plates and deep mantle flow? Many studies have attempted to model plate tectonics (through the torque balance method or through calculating the lithospheric stress field) as a mere lithospheric process, independent of active deeper density buoyancy-driven convective flow in the mantle [*Solomon et al.*, 1975; *Richardson et al.*, 1979; *Sandiford and Coblentz*, 1994]. On the other hand, various other studies have considered mantle convection and plate tectonics as a single system in order to explain the plate tectonic phenomenon [*Bercovici*, 1995, 1998; *Tackley*, 1998, 2000; *Trompert and Hansen*, 1998] or to explain observables such as the geoid, dynamic topography, and plate motions [*Hager*, 1984; *Hager et al.*, 1985; *Richards and Hager*, 1984; *Gable et al.*, 1991; *Forte et al.*, 1993; *Zhang and Christensen*, 1993; *Wen and Anderson*, 1997b, 1997c; *Thoraval and Richards*, 1997; *Zhong and Davies*, 1999; *Becker and O'Connell*, 2001; *Zhong*, 2001; *Moucha et al.*, 2007; *Kaban et al.*, 2007; *Tosi et al.*, 2009; *Yoshida and Nakakuki*, 2009; *Ghosh et al.*, 2010; *Forte et al.*, 2010a, 2010b]. However, the problem with directly relating mantle convection with plate tectonics is that the latter is not strictly a fluid dynamical process, as evident from the existence of nearly rigid plates. In this paper, we seek to address the role and nature of lithosphere-mantle coupling by performing a joint modeling of lithosphere dynamics and mantle convection. Two important observations that are sensitive to the nature of plate-mantle coupling are the lithospheric deviatoric stress field and plate motions. If the initial coupling model is correct, the predicted deviatoric stress tensor field will match

All Supporting Information may be found in the online version of this article.

[1]Department of Geosciences, Stony Brook University, Stony Brook, New York, USA.
[2]Now at Centre for Earth Sciences, Indian Institute of Science, Bangalore, India.
[3]Laboratory of Seismology and Physics of Earth's Interior, University of Science and Technology of China, Hefei, Anhui, China.

Corresponding author: A. Ghosh, Centre for Earth Sciences, Indian Institute of Science, Bangalore 560012, India. (atreig@gmail.com)

2169-9313/13/2012JB009516

deformation indicators, and the predicted surface motions will also match the observed plate motions. However, use of either one of these constraints, by itself, leads to nonunique inferences about the plate-mantle coupling system. That is, a particular coupling model may satisfy one constraint but not the other. Hence, both of these constraints are necessary to delineate a coupling model for the Earth.

[3] The prediction of the Earth's lithospheric stress field, as well as its plate motions, is largely influenced by the distribution of density buoyancies as well as radial and lateral variation of viscosities in the lithosphere and the mantle. In the past, there have been studies that investigated this lithosphere-mantle coupling problem [*Bai et al*., 1992; *Bird*, 1998; *Steinberger et al*., 2001; *Lithgow-Bertelloni and Guynn*, 2004; *Ghosh et al*., 2008; *Bird et al*., 2008; *Naliboff et al*., 2009; *Ghosh and Holt*, 2012] by jointly modeling lithosphere and mantle dynamics and predicting the lithospheric stress field. *Bai et al*. [1992] were the first to perform such a joint modeling. They used the intraplate stress field to evaluate their models. However, they failed to achieve a good correlation between their predicted stresses and observed stress directions. *Bird* [1998] utilized a thin sheet method with faults at plate boundaries and temperature-dependent viscous rheology in his approach to model the lithospheric stress field. He concluded that basal driving tractions were necessary to match the observed stress field. *Steinberger et al*. [2001] computed the global stress field from mantle convection based on global seismic tomography and added it to the contribution from intralithospheric sources. They, on the other hand, found that predicted stress directions with or without mantle flow matched stress observations equally well. They also predicted plate motions in addition to predicting the intraplate stress field. *Lithgow-Bertelloni and Guynn* [2004] performed a joint modeling of lithospheric and mantle sources of stress and explored the effects of radial changes in viscosity in the mantle. Like *Bird* [1998], they too argued for importance of basal tractions. *Ghosh et al*. [2008] performed similar joint modeling using solutions to depth integrated three-dimensional (3-D) force balance. They found that stresses from basal tractions, arising due to density driven mantle convection, when added to stresses from topography and shallow lithospheric sources, yield a better fit to deformation indicators along the Earth's plate boundary zones. They also tested the sensitivity of different radially variable viscosity structures and argued for strong lithosphere-asthenosphere viscosity contrasts. Excluding the first and last-mentioned study, all the other studies used the World Stress Map (WSM) [*Zoback*, 1992; *Heidbach et al*., 2008] to constrain their modeled lithospheric stress field. *Ghosh et al*. [2008], on the other hand, used the velocity gradient tensor field along the deforming plate boundary zones from the Global Strain Rate Map (GSRM) [*Kreemer et al*., 2003] to constrain their predicted stresses. None of the above studies, however, investigated lateral variation in both lithosphere and asthenosphere viscosity. *Naliboff et al*. [2009] looked particularly at the effects of lateral viscosity variations on plate-mantle coupling. They concluded that the presence of cratonic roots do not have a significant effect on stress magnitudes and pattern in the overlying lithosphere. However, they did not compare their results with any observational constraint. The addition of lateral variation of viscosity also enables one to adequately predict plate motions. It is thus important to satisfy both the deformation constraint and the plate motion constraint in order to delineate the best plate-mantle coupling model. *Ghosh and Holt* [2012] looked at predictions of deviatoric stresses and plate motions using similar joint modeling method as in *Ghosh et al*. [2008], except that they tested lateral viscosity variations in the lithosphere and upper mantle. In this study we further quantify the sensitivity of plate motions and stresses to lateral viscosity variations. We also quantify driving versus resistive tractions on the Earth's surface and present a complete model for the motions of the major plates.

[4] We compute the lithospheric stress field from sources within the lithosphere and from a full 3-D mantle flow field, driven by density buoyancies within the mantle that includes both radial and lateral viscosity variations. We compare our solutions with the plate motion model of *Kreemer et al*. [2006] defined by GPS observations, with strain rate information from GSRM, and with $SH_{\max}$ (most compressive principal stress axes) directions from the WSM. Plate velocities consist of both poloidal and toroidal components. The poloidal component is associated with upwelling (divergence) in mid-oceanic ridges and downwelling (convergence) in subduction zones, whereas the toroidal component is related to strike-slip faulting along transform fault boundaries. We generate plate motions self-consistently from our convection models, instead of placing them as a priori boundary conditions. The combination of predicting lithospheric stress field and plate motions enables us to investigate the nature of plate-mantle coupling. Another important contribution of the present study is the matching of the relative toroidal and poloidal flow magnitudes. Barring a few studies, matching the toroidal/poloidal velocity ratio has proved to be a difficult problem in studies of mantle convection (discussed in section 4.2). In this study, we not only attempt to match the direction of plate velocities, but also their relative magnitudes via the computation of the toroidal/poloidal velocity ratio. A very important consequence of using all the three constraints of lithospheric stress field, plate motions, and the toroidal/poloidal velocity ratio is the elimination of a wide range of viscosity models that fail to satisfy these constraints simultaneously.

2. Method

[5] On a longer timescale, plates behave as viscous bodies and flow horizontally under their own weight. *Frank* [1972] drew the analogy of the Earth's lithospheric motion to the flow in glaciers. Lateral density variations within the lithosphere, along with varying crustal thickness and topography, give rise to gravitational potential energy per unit area (GPE) differences. A higher elevation column of lithosphere stores more GPE than a lower elevation column of the same density. The horizontal gradients in GPE produce deviatoric stresses that give rise to horizontal flow from points of high GPE to points of low GPE. Effects of these density variations within the lithosphere have been studied by *Artyushkov* [1973], *Fleitout and Froidevoux* [1982], *Fleitout and Froidevoux* [1983], *Fleitout* [1991], *Richardson* [1992], and *Coblentz et al*. [1994], amongst many others. On the other hand, mantle convection can be envisaged as a fluid dynamical process whereby the flow is driven by sources of buoyancy deep into the mantle (mostly subducted slabs). These buoyancy sources lead to convection on a variety of scales, which give rise to basal tractions that act at the base of the

lithosphere and contribute to the lithospheric stress field. To date, the most efficient way to address the full problem is to separate it into two parts: (1) the contribution of GPE differences and (2) the contribution of coupling with 3-D mantle flow. We separately calculate these two contributions through solutions to depth-integrated 3-D force balance in a finite element model of the lithosphere that possesses detailed lateral viscosity variations. Tractions arising from 3-D mantle convection act as a basal boundary condition in the lithosphere finite element model. The solutions of GPE and tractions are then combined to obtain the full model. We show with benchmarking tests that this method is an accurate and efficient means to explore a wide range of models. Breaking the problem into two parts also allows us to quantify the relative contribution of coupling with mantle flow versus the contribution of detailed topography and lithosphere structure, which is a controversial issue.

2.1. Depth Integration of 3-D Force Balance Equations

[6] The force balance equations, in spherical coordinates, are given as [*Ghosh et al.*, 2008],

$$\frac{1}{\cos\theta}\frac{\partial}{\partial\varphi}\left(r^2\sigma_{\varphi\varphi}\right)+\frac{1}{\cos^2\theta}\frac{\partial}{\partial\theta}\left(r^2\sigma_{\varphi\theta}\cos^2\theta\right)+\frac{\partial}{\partial r}\left(r^3\sigma_{\varphi r}\right)=0 \quad (1)$$

$$\frac{1}{\cos\theta}\frac{\partial}{\partial\varphi}\left(r^2\sigma_{\varphi\theta}\right)+\frac{1}{2}\frac{\partial}{\partial\theta}\left(r^2\left[\sigma_{\theta\theta}+\sigma_{\varphi\varphi}\right]\right)+\frac{1}{2\cos^2\theta}\frac{\partial}{\partial\theta}\left(r^2\cos^2\theta\left[\sigma_{\theta\theta}-\sigma_{\varphi\varphi}\right]\right)+\frac{\partial}{\partial r}\left(r^3\sigma_{\theta r}\right)=0 \quad (2)$$

$$\frac{1}{r\cos\theta}\frac{\partial\sigma_{\varphi r}}{\partial\varphi}+\frac{1}{r\cos\theta}\frac{\partial}{\partial\theta}\left(\cos\theta\sigma_{\theta r}\right)+\frac{1}{r}\left(2\sigma_{rr}-\sigma_{\varphi\varphi}-\sigma_{\theta\theta}\right)+\frac{\partial\sigma_{rr}}{\partial r}-\rho g=0 \quad (3)$$

where r is the radius of the Earth, ρ is the density, g is the gravitational acceleration, σ_{ij} are the total stresses, θ is latitude, and φ is longitude. Vertically integrating (1) and (2) and substituting the total stress tensor, σ_{ij}, by the deviatoric stress tensor, τ_{ij}, via $\sigma_{ij}=\tau_{ij}+\frac{1}{3}\sigma_{kk}\delta_{ij}$, we arrive at

$$\frac{1}{\cos\theta}\frac{\partial}{\partial\varphi}\left(\int_{r_L}^{r_0}r^2\tau_{\varphi\varphi}\mathrm{d}r\right)-\frac{1}{\cos\theta}\frac{\partial}{\partial\varphi}\left(\int_{r_L}^{r_0}r^2\tau_{rr}\mathrm{d}r\right)+\frac{1}{\cos^2\theta}\frac{\partial}{\partial\theta}\left(\cos^2\theta\int_{r_L}^{r_0}r^2\tau_{\varphi\theta}\mathrm{d}r\right)=-\frac{1}{\cos\theta}\frac{\partial}{\partial\varphi}\left(\int_{r_L}^{r_0}r^2\sigma_{rr}\mathrm{d}r\right)-r_0^3\tau_{\varphi r}(r_0)+r_L^3\tau_{\varphi r}(r_L) \quad (4)$$

and

$$\frac{1}{\cos\theta}\frac{\partial}{\partial\varphi}\left(\int_{r_L}^{r_0}r^2\tau_{\varphi\theta}\mathrm{d}r\right)+\frac{1}{2}\frac{\partial}{\partial\theta}\left(\int_{r_L}^{r_0}r^2\tau_{\theta\theta}\mathrm{d}r+\int_{r_L}^{r_0}r^2\tau_{\varphi\varphi}\mathrm{d}r\right)+\frac{\partial}{\partial\theta}\left(\int_{r_L}^{r_0}r^2\tau_{rr}\mathrm{d}r\right)+\frac{1}{2\cos^2\theta}\frac{\partial}{\partial\theta}\left(\cos^2\theta\left[\int_{r_L}^{r_0}r^2\tau_{\theta\theta}\mathrm{d}r-\int_{r_L}^{r_0}r^2\tau_{\varphi\varphi}\mathrm{d}r\right]\right)=-\frac{\partial}{\partial\theta}\left(\int_{r_L}^{r_0}r^2\sigma_{rr}\mathrm{d}r\right)-r_0^3\tau_{\theta r}(r_0)+r_L^3\tau_{\theta r}(r_L) \quad (5)$$

[7] Here, r_0 is the radius from the center of the Earth to the surface, r_L is the radius from the center to a constant reference level, and δ_{ij} is the Kronecker delta. Because horizontal tractions at the surface, $\tau_{r\varphi}(r_0)$, $\tau_{r\theta}(r_0)$, are zero, the integral of the last term in equations (1) and (2) yields the horizontal tractions, $r_L^3\tau_{\varphi r}(r_L)$ and $r_L^3\tau_{\theta r}(r_L)$, acting at the reference level r_L. Density driven mantle convection plays a fundamental role in generating these tractions. As long as the depth integral of horizontal tractions is small in comparison with the depth integrals of horizontal deviatoric stress, it is appropriate to seek solutions to equations (4) and (5) [*Ghosh et al.*, 2009]. The first term on the right-hand side of equations (5) and (6) represents horizontal gradients in the depth integrals of vertical stress, or GPE. As such, the gradients in GPE and the tractions acting at the reference level, r_L, constitute body-force-like terms, and are constrained by observations: GPE by topography and a seismically-defined crustal thickness dataset (Crust 2.0), and tractions by a self-consistent whole mantle circulation model [*Wen and Anderson*, 1997b] that is described in the next section.

[8] The approximation that we make, which could be called the approximation that underlies the "thin sheet" approach, is that the gradients of $\sigma_{\varphi r}$ and $\sigma_{\theta r}$ in equation (3) are negligibly small as is the term $\frac{1}{r}\left(2\sigma_{rr}-\sigma_{\varphi\varphi}-\sigma_{\theta\theta}\right)$ compared to ρg. Hence, equation (3) can be approximated as

$$\sigma_{rr}=-\int_r^{r_0}\rho g\mathrm{d}r, \quad (6)$$

so that the GPE equation is given by

$$\int_{r_L}^{r_0}r^2\sigma_{rr}\mathrm{d}r=-\int_{r_L}^{r_0}r^2\left[\int_r^{r_0}\rho g\mathrm{d}r'\right]\mathrm{d}r=-\int_{r_L}^{r_0}\rho g\left[\int_{r_L}^{r'}r^2\mathrm{d}r\right]\mathrm{d}r'=-\int_{r_L}^{r_0}\frac{1}{3}\rho g\left(r'^3-r_L^3\right)\mathrm{d}r' \quad (7)$$

based on a reference level at depth r_L. We take r_L to be 100 km below sea-level. In the estimation of lithosphere GPE we do not take into account deeper lithospheric buoyancies arising from cratonic roots; instead, they are considered part of the convection problem. In order to consider these deeper lithospheric buoyancies in the lithospheric calculation of GPE, a variable base lithosphere needs to be accounted for, which involves sophisticated methods that are beyond the scope of this paper. In oceans, r_0 constitutes sea-level and hence is constant, whereas it varies in continents in accordance with varying topography. Given the GPE differences, solutions to (4) and (5) can be obtained with $\tau_{\varphi r}$ and $\tau_{\theta r}$ set to zero. Alternatively, given the basal tractions, gradients in GPE (7) can be set to zero in order to compute the stress response from basal tractions. The two contributions from each set of forcings are added to obtain the total lithospheric stress field, as the equations are linear in stress. We use a finite element technique [*Flesch et al.*, 2001] on a global grid of $1°\times1°$ such that the deviatoric stress field solution provides a global minimum in the second invariant of deviatoric stress, taking into account rheological variations due to strong plates and weak plate boundaries. Based on the strain rates from GSRM, the plate boundaries are assigned variable viscosities using the method of *Ghosh et al.* [2009],

$$\frac{1}{\mu} = 1 + \left(\frac{1}{\mu_{\mathrm{ref}}} - 1\right)\sqrt{\frac{E^2}{E_{\mathrm{ref}}^2}}, \tag{8}$$

where $E^2 = 2\left(\dot{\varepsilon}_{\theta\theta}^2 + \dot{\varepsilon}_{\varphi\varphi}^2 + \dot{\varepsilon}_{\varphi\theta}^2 + \dot{\varepsilon}_{\varphi\varphi}\dot{\varepsilon}_{\theta\theta}\right)$, and $\dot{\varepsilon}_{\theta\theta}, \dot{\varepsilon}_{\varphi\varphi}$ and $\dot{\varepsilon}_{\varphi\theta}$ are the strain rates from *Kreemer et al.* [2003]. A reference viscosity is assigned to a moderately straining region in western North America (straining at a rate of 1.5×10^{-7}/yr) having an effective viscosity ~ 30 times lower than the nondeforming intraplate regions. E_{ref}^2 is the reference value for E^2 corresponding to the value for μ_{ref}. From these modeled deviatoric stresses, we can also calculate strain rates and plate velocities.

[9] The GPE in equation (8) is calculated from the crustal thickness and density dataset in Crust 2.0 [*G. Laske et al.*, Crust 2.0: A new global crustal model at 2 × 2 degrees, 2002, available at http://mahi.ucsd.edu/Gabi/rem.html]; the densities in the oceanic lithosphere are defined by the cooling plate model based on ocean floor age data [*Müller et al.*, 2008, 1997] with revised parameters from *Stein and Stein* [1992].

2.2. Mantle Convection Treatment for Generating Traction Boundary Conditions

[10] The basal tractions that are applied as basal boundary conditions in the finite element model (solution to equations (5) and (6)) are obtained from a separate whole mantle convection model and the methodology of [*Wen and Anderson*, 1997b], assuming an incompressible Newtonian viscous fluid with zero Reynold's number. The flow is driven by tomography and history of subduction. The governing equations are the equation of continuity,

$$\nabla \cdot U = 0, \tag{9}$$

[11] U being the surface velocity, the equation of motion,

$$\nabla \cdot \tau + \delta\rho g = 0, \tag{10}$$

and the constitutive equation between stress and strain rate,

$$\tau = -p + 2\eta\varepsilon. \tag{11}$$

[12] Here τ is the stress tensor, $\delta\rho$ the density anomaly, g the acceleration due to gravity, p the pressure, η the viscosity and ε the strain rate tensor. The variables are expanded in terms of spherical harmonics. For a radially symmetric viscosity structure, poloidal-poloidal, poloidal-toroidal, and toroidal-toroidal equations are decoupled at every spherical harmonic degree and order [*Kaula*, 1975; *Hager and O'Connell*, 1981]. For a laterally variable viscosity structure, poloidal and toroidal equations are coupled at each degree and order [*Wen and Anderson*, 1997b]. If the coefficients are truncated at a certain spherical harmonic degree, the above equations can be reduced to a set of linear equations and can be solved in three dimensions using a semispectral iterative method [*Karpychev and Fleitout*, 1996]. The boundary conditions are free-slip at the surface and at core-mantle boundary (CMB). Our mantle convection models include both radial and lateral variations of viscosity, with the lower mantle being 10 times more viscous than the upper mantle. The density anomalies in the upper mantle are inferred by adjusting the relative weights of density anomalies related to subducting slabs and residual tomography [*Wen and Anderson*, 1997a] on the basis of fitting the geoid. The density structure in the lower mantle was derived from a seismic tomographic model [*Su et al.*, 1994]. With latitude θ as positive north latitude, the basal tractions can be given as

$$r_L(\tau_{\varphi r})/\eta_0 = Z_4^{lm}\frac{1}{\cos\theta}\frac{\partial}{\partial\varphi}Y_{lm}(\theta,\varphi) + Z_6^{lm}\frac{\partial}{\partial\theta}Y_{lm}(\theta,\varphi) \tag{12}$$

$$r_L(\tau_{\theta r})/\eta_0 = Z_4^{lm}\frac{\partial}{\partial\theta}Y_{lm}(\theta,\varphi) - Z_6^{lm}\frac{1}{\cos\theta}\frac{\partial}{\partial\varphi}Y_{lm}(\theta,\varphi) \tag{13}$$

where η_0 is the reference viscosity, Z_4^{lm} and Z_6^{lm} are the spherical harmonic coefficients for the poloidal and toroidal components of stress (defined in *Wen and Anderson* [1997b]), $Y_{lm}(\theta,\varphi)$ is the surface normalized spherical harmonic of degree l and order m, whose maximum value is 31 in this study. The horizontal velocities are given by

$$U_\varphi = Z_2^{lm}\frac{1}{\cos\theta}\frac{\partial Y_{lm}(\theta,\varphi)}{\partial\varphi} + Z_5^{lm}\frac{\partial Y_{lm}(\theta,\varphi)}{\partial\theta} \tag{14}$$

$$U_\theta = Z_2^{lm}\frac{\partial Y_{lm}(\theta,\varphi)}{\partial\theta} - Z_5^{lm}\frac{1}{\cos\theta}\frac{\partial Y_{lm}(\theta,\varphi)}{\partial\varphi} \tag{15}$$

where Z_2 and Z_5 are the poloidal and toroidal components of velocity, expressed as divergence ($\nabla \cdot U$) and vorticity ($\nabla \times U$, U being the velocity). Using a solution method described below, tractions from the convection model are output at a constant reference level, r_L, and then applied below a laterally variable lithosphere of much higher resolution (1 × 1 degree) in a finite element model to yield estimates of the depth integral of deviatoric stress associated with these tractions.

[13] We experiment with various radially symmetric, as well as laterally variable viscosity structures (Table 1). Note that the truncation degree is quite low in our study ($l = 31$) and hence, small scale features are missing in our convection model. We are therefore investigating the contribution of long-wavelength components of density driven mantle flow, which generates basal tractions at the reference level r_L. The lateral viscosity variations in the finite element lithosphere model, discussed next, in which the depth integral predictions of deviatoric stress are performed, is of much higher resolution (1 × 1 degree). The main goal of the study is to explain the first order features of generating plate motion and lithosphere deviatoric stress by a simple model, and not to match all the detailed features of these, which would require much higher resolution and sophisticated models for both the mantle flow and lithosphere stress predictions.

2.3. Solving for Depth Integrated Deviatoric Stresses in the Lithosphere Associated With Basal Tractions and GPE Differences

[14] Our finite element solution provides depth integrals of deviatoric stress that both balance the body force distributions and simultaneously constitute a global minimum of the

Table 1. Results From Our Various Viscosity Models[a]

	Viscosity								Plate Motions		
	0–100				100–200		200–400		RMS (cm/y)	P/P'	T/T'
Model	lith	c	o	wz	c	asth	asth	Stress			
1	100	1000	0	0	10	0.01	0.01	0.80	1.20	0.92	0.89
2	100	1000	0	0	1	0.01	0.01	0.82	1.09	0.93	0.90
3	100	1000	0	0	0.1	0.01	0.01	0.82	1.07	0.93	0.91
4	100	1000	0	0	0	0.01	0.01	0.82	1.06	0.94	0.91
5	100	1000	0	0	100	0.1	0.1	0.82	1.21	0.87	0.82
6	100	1000	0	0	10	0.1	0.1	0.85	1.03	0.87	0.82
7	100	1000	0	0	1	0.1	0.1	0.85	1.01	0.94	0.92
8	100	1000	0	0	0	0.1	0.1	0.85	1.01	0.94	0.92
9	100	10000	0	0	0	0.01	0.01	0.82	1.06	0.93	0.91
10	100	10000	0	0	0	0.1	0.1	0.85	1.02	0.94	0.92
11	10	100	0	0	10	1	1	0.70	1.56	0.78	0.64
12	10	100	0	0	10	0.1	0.1	0.82	1.02	0.95	0.93
13	10	100	0	0	1	0.1	0.1	0.82	1.03	0.89	0.86
14	10	100	0	0	0	0.1	0.1	0.82	1.03	0.87	0.82
15	10	100	0	0	0	0.01	0.01	0.81	1.03	0.87	0.82
16	1	100	0	0	0	0.01	0.01	0.78	1.10	0.94	0.90
17	100	0	1000	0	0	0.01	0.01	0.82	1.06	0.93	0.91
18	100	0	1000	0	0	0.1	0.1	0.85	1.01	0.94	0.92
19	10	0	100	0	0	0.01	0.01	0.81	1.05	0.94	0.91
20	10	0	100	0	0	0.1	0.1	0.82	1.10	0.93	0.91
21	1	0	10	0	0	0.01	0.01	0.71	1.35	0.89	0.86
22	1	0	10	0	0	0.1	0.1	0.22	3.30	0.08	0.26
23	1	0	100	0	0	0.1	0.1	0.51	2.77	0.36	0.49
24	1	0	100	0	0	0.01	0.01	0.76	1.27	0.91	0.87
25	100	0	0	sr	0	0.01	0.01	0.82	1.06	0.93	0.91
26	10	0	0	sr	0	0.01	0.01	0.80	1.04	0.94	0.91
27	10	0	0	sr	0	0.1	0.1	0.75	1.18	0.94	0.91
28	1	0	0	sr	0	0.1	0.1	0.08	3.53	0.04	0.18
29	1	0	0	sr	0	0.01	0.01	0.63	1.49	0.88	0.84
30	100	1000	1000	0	10	0.1	0.1	0.85	1.04	0.94	0.92
31	100	1000	1000	0	1	0.1	0.1	0.85	1.01	0.94	0.92
32	100	1000	1000	0	1	0.01	0.01	0.82	1.09	0.93	0.90
33	10	100	100	0	100	0.1	0.1	0.78	1.32	0.91	0.88
34	10	100	100	0	10	0.1	0.1	0.83	1.04	0.94	0.92
35	10	100	100	0	1	0.01	0.01	0.82	1.07	0.93	0.90
36	1	100	10	0	0	0.01	0.01	0.79	1.06	0.94	0.89
37	100	1000	0	sr	1	0.1	0.1	0.85	1.01	0.94	0.92
38	100	1000	0	sr	0.1	0.01	0.01	0.82	1.07	0.93	0.91
39	10	100	0	sr	10	0.1	0.1	0.83	1.06	0.94	0.92
40	10	100	0	0.1	10	0.1	0.1	0.82	1.03	0.94	0.92
41	10	100	0	0.1	1	0.1	0.1	0.82	1.05	0.94	0.91
42	10	0	100	sr	0	0.1	0.1	0.83	1.03	0.94	0.92
43	10	0	100	sr	0	0.01	0.01	0.81	1.05	0.94	0.91
44	100	0	1000	sr	0	0.01	0.01	0.82	1.06	0.93	0.91
45	100	0	1000	sr	0	0.1	0.1	0.85	1.01	0.94	0.92
46	100	1000	1000	sr	10	0.1	0.1	0.85	1.05	0.94	0.92
47	100	1000	1000	sr	1	0.1	0.1	0.85	1.01	0.94	0.92
48	100	1000	1000	sr	0	0.1	0.1	0.85	1.01	0.94	0.92
49	100	1000	1000	sr	1	0.01	0.01	0.82	1.10	0.93	0.90
50	100	1000	1000	sr	0.1	0.01	0.01	0.82	1.07	0.93	0.91
51	100	1000	1000	sr	0	0.01	0.01	0.82	1.06	0.93	0.91
52	10	100	100	0.1	10	0.1	0.1	0.83	1.05	0.94	0.91
53	10	100	100	0.1	1	0.1	0.1	0.83	1.03	0.94	0.91
54	10	100	100	0.1	0.1	0.01	0.1	0.82	1.02	0.93	0.90

[a]The three columns under Viscosity denote the depth of occurrence of lateral viscosity variations (between 0–400 km). lith, c, o, and wz stand for lithosphere, continental cratonic regions, old oceanic lithosphere, and weak zones, respectively. sr stands for strain rate dependent viscosity. The reference viscosity is 10^{21} Pa-s. Hence, a value of 10 would mean an absolute viscosity of 10^{22} Pa-s. A value of 0 would mean no viscosity variation due to that particular feature. The column next to Viscosity (labeled Stress) indicates correlation coefficients between strain rate tensor field from GSRM and predicted deviatoric stress fields from combined GPE plus tractions. The column RMS indicates the RMS misfit (cm/yr calculated at every degree for 63,000 points on Earth) between the predicted dynamic surface velocities and kinematic velocities (from *Kreemer et al.* [2006]). The P/P' and T/T' under Plate Motions denote the average correlation coefficients up to spherical harmonic degree 20 between the dynamic and kinematic (from *Kreemer et al.* [2006]) patterns of poloidal and toroidal velocity. Hence, for example, the second row (model 1) implies that the lateral viscosity variations in the top 100 km is only due to the presence of higher viscosity cratonic regions that are 1000 times that of reference viscosity with a lithosphere 100 times stronger than reference viscosity. Below 100 km the cratons possess a viscosity that is 10 times stronger than the reference viscosity between the depths of 100–200 km. Outside of cratonic regions between 100–200 km depth, and everywhere between 200–400 km depth, the asthenosphere possesses a viscosity 100 times weaker than reference viscosity.

second invariant of deviatoric stress. This is accomplished through minimization of the following functional [*Flesch et al.*, 2001]:

$$
\begin{aligned}
I = & \iint \frac{1}{\mu}\left[\bar{\tau}_{\varphi\varphi}^2 + 2\bar{\tau}_{\varphi\theta}^2 + \bar{\tau}_{\theta\theta}^2 + \left(\bar{\tau}_{\varphi\varphi} + \bar{\tau}_{\theta\theta}\right)^2\right]\cos\theta \mathrm{d}\varphi \mathrm{d}\theta \\
& + \iint \left\{ 2\lambda_\varphi \left[\frac{1}{\cos\theta}\frac{\partial\bar{\tau}_{\varphi\varphi}}{\partial\varphi} + \frac{1}{\cos\theta}\frac{\partial}{\partial\varphi}\left(\bar{\tau}_{\varphi\varphi} + \bar{\tau}_{\theta\theta}\right) \right.\right. \\
& \left. + \frac{1}{\cos^2\theta}\frac{\partial}{\partial\theta}\left(\cos^2\theta\bar{\tau}_{\varphi\theta}\right) + \frac{1}{\cos\theta}\frac{\partial\bar{\sigma}_{rr}}{\partial\varphi} - r_L^3\sigma_{\varphi r}(r_L)\right] \\
& + 2\lambda_\theta \left[\frac{1}{\cos\theta}\frac{\partial\bar{\tau}_{\varphi\theta}}{\partial\varphi} + \frac{3}{2}\frac{\partial}{\partial\theta}\left(\bar{\tau}_{\theta\theta} + \bar{\tau}_{\varphi\varphi}\right) \right. \\
& + \frac{1}{2\cos^2\theta}\frac{\partial}{\partial\theta}\left(\cos^2\theta\left[\bar{\tau}_{\theta\theta} - \bar{\tau}_{\varphi\varphi}\right]\right) \\
& \left.\left. + \frac{\partial\bar{\sigma}_{rr}}{\partial\theta} - r_L^3\sigma_{\theta r}(r_L)\right]\right\}\cos\theta d\varphi d\theta
\end{aligned}
\quad (16)
$$

where $\bar{\tau}_{\varphi\varphi}$, $\bar{\tau}_{\theta\theta}$, and $\bar{\tau}_{\varphi\theta}$ are the vertically integrated deviatoric stresses, $\bar{\sigma}_{rr}$ is the vertically integrated total vertical stress, λ_φ, λ_θ represent the horizontal components of the Lagrange multipliers for the force balance equation constraint, and μ is the relative viscosity, which varies laterally in order to take into account weak plate boundaries and strong plates in the lithosphere model (equation (8)). The body force equivalents that go into making up the potentials are distributions of GPE and distributions of the negative of the tractions. It should be noted that the stress magnitudes within the global force balance, as well as the orientations and styles of those stresses, are primarily controlled by the effective body forces, and only weakly controlled by relative viscosities. Optimizing equation (16) yields a relation between the deviatoric stresses, $\tau_{\alpha\beta}$, and the Lagrange multipliers, λ_φ and λ_θ [*Flesch et al.*, 2001]

$$\bar{\tau}_{\varphi\varphi} = \mu\left(\frac{1}{\cos\theta}\frac{\partial\lambda_\varphi}{\partial\varphi} - \lambda_\theta\tan\theta\right), \quad (17)$$

$$\bar{\tau}_{\theta\theta} = \mu\frac{\partial\lambda_\theta}{\partial\theta}, \quad (18)$$

$$\bar{\tau}_{\varphi\theta} = \frac{\mu}{2}\left(\frac{\partial\lambda_\varphi}{\partial\theta} + \frac{1}{\cos\theta}\frac{\partial\lambda_\theta}{\partial\varphi} + \lambda_\varphi\tan\theta\right). \quad (19)$$

[15] Note that the relation between τ and the Lagrange multipliers, $\lambda_\varphi, \lambda_\theta$, is identical to the relation between strain rate and velocities. Substitution of 17–19 into $\bar{\tau}_{\varphi\varphi}, \bar{\tau}_{\theta\theta}$, and $\bar{\tau}_{\varphi\theta}$ in the following J functional, and then minimization of J with respect to λ_φ and λ_θ provides a solution to the force balance in equations (2) and (3), where J is

$$
\begin{aligned}
J = \iint \Bigg\{ & \left[\begin{pmatrix}\bar{\tau}_{\varphi\varphi}\\ \bar{\tau}_{\theta\theta}\\ \bar{\tau}_{\varphi\theta}\end{pmatrix} - \begin{pmatrix}\Phi_{\varphi\varphi}^{obs}\\ \Phi_{\theta\theta}^{obs}\\ \Phi_{\varphi\theta}^{obs}\end{pmatrix}\right]^T \\
& \widetilde{V}^{-1}\left[\begin{pmatrix}\bar{\tau}_{\varphi\varphi}\\ \bar{\tau}_{\theta\theta}\\ \bar{\tau}_{\varphi\theta}\end{pmatrix} - \begin{pmatrix}\Phi_{\varphi\varphi}^{obs}\\ \Phi_{\theta\theta}^{obs}\\ \Phi_{\varphi\theta}^{obs}\end{pmatrix}\right]\Bigg\}\cos\theta \mathrm{d}\varphi \mathrm{d}\theta.
\end{aligned}
\quad (20)
$$

[16] Here $\bar{\tau}_{\varphi\varphi}, \bar{\tau}_{\theta\theta}$, and $\bar{\tau}_{\varphi\theta}$ are the depth integrated deviatoric stresses we are solving for, $\Phi_{\varphi\varphi}^{obs}$, $\Phi_{\theta\theta}^{obs}$, and $\Phi_{\varphi\theta}^{obs}$ are the potentials consisting of horizontal integrals of the body force equivalents and $\widetilde{V}$ is the variance-covariance matrix [see *Ghosh et al.*, 2008, Appendix B]. For calculation of the depth integrals of deviatoric stress, we solve equations (4) and (5), given distributions of GPE, $\frac{1}{\cos\theta}\frac{\partial\bar{\sigma}_{rr}}{\partial\varphi}$ and $\frac{\partial\bar{\sigma}_{rr}}{\partial\theta}$, and given distributions of the negative of the tractions, $-r_L^3\sigma_{\varphi r}(r_L)$ and $-r_L^3\sigma_{\theta r}(r_L)$, obtained from mantle convection models.

2.4. Treatment of Radial Tractions or Dynamic Topography

[17] The tangential tractions, $\tau_{\varphi r}$ and $\tau_{\theta r}$ in equations (12) and (13), arise from the horizontal component of the 3-D convective flow. The vertical component, τ_{rr}, that gives rise to dynamic topography, could potentially play an important role in affecting the total deviatoric stress field. In this section, we will discuss ways of incorporating these radial tractions in our calculation.

[18] There are two ways of dealing with the radial tractions [*Ghosh et al.*, 2008]. One way is to calculate them as part of the lithospheric contribution. The other way is to predict them from the mantle convection models. We will first discuss the method that treats radial tractions as part of the lithospheric contribution. The observed topography is a combination of both static and dynamic parts. The former is generated by shallow density buoyancies within the lithosphere, whereas the latter is produced by deeper density buoyancies within the mantle. Hence, the depth integrals of σ_{rr} for the observed topography, down to a constant reference level (r_L), already contain contributions from both static and dynamic parts. In this case, the density variations are obtained from a seismically constrained crust and upper mantle structure that is uncompensated. Although the contribution from dynamic topography is not explicitly known, it is implicitly included in the calculation of the depth integral of σ_{rr}.

[19] The second way is to treat the radial tractions as part of the convection problem. From the dynamic topography predicted by the respective convection models, the GPE differences and the associated deviatoric stress field can be calculated. This stress field is the response of the radial tractions. These stresses can then be added to the stresses obtained from tangential tractions, $\tau_{\varphi r}$ and $\tau_{\theta r}$, in order to obtain the total stress field produced by the convection model. This combined stress field is then added to the deviatoric stresses from a compensated (equal pressure at the reference level, r_L) lithosphere model in order to obtain a total lithospheric deviatoric stress field. The lithosphere model must be compensated via elevation adjustment of the crustal columns (removal of dynamic topography) such that after the adjustment, the pressure at the reference level, r_L, is constant. Hence, this method deals with the additional step of compensating the Crust 2.0 model by removing an estimate of dynamic topography. Although the second method is a more self-consistent way of treating the radial component of the mantle flow field, there are other problems involved in this methodology. First, the compensation of the crustal model is likely to introduce errors. For complete self-consistency, the dynamic topography predicted by the convection model should be identical to the dynamic topography computed

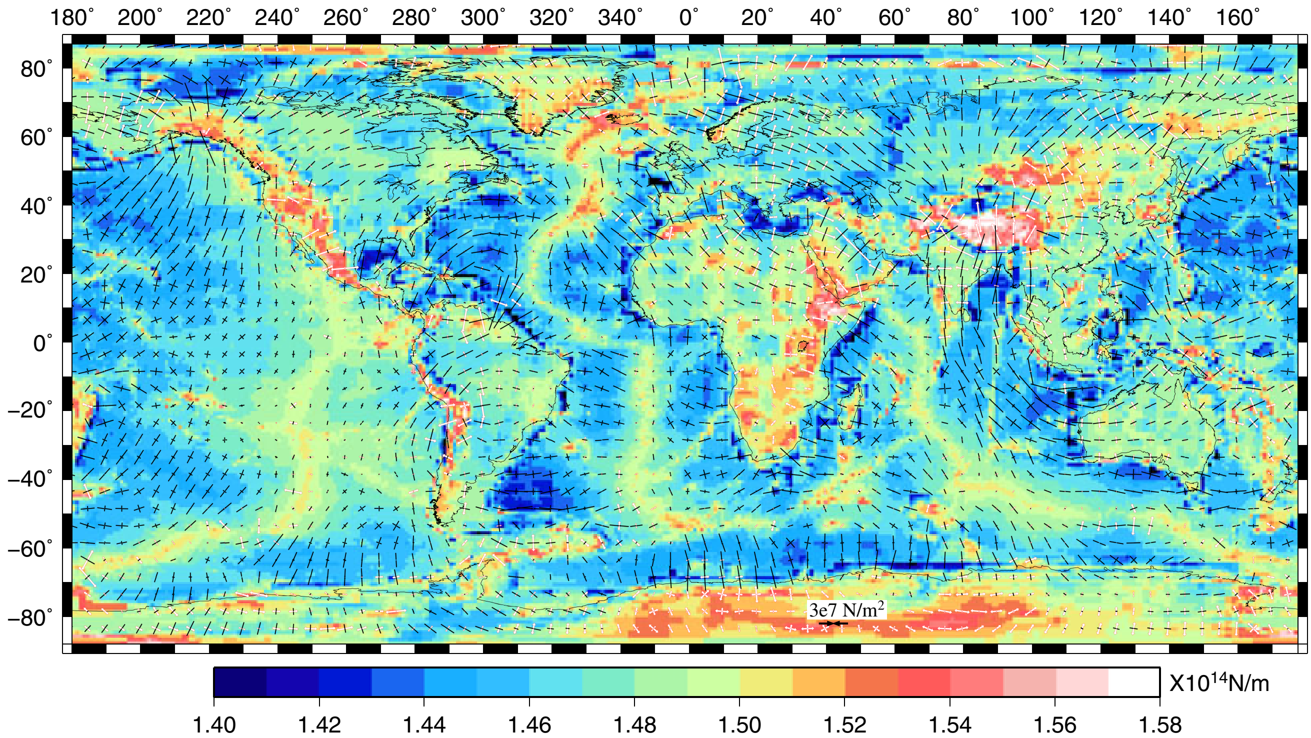

Figure 1. Deviatoric stress distribution plotted at every 5° on GPE calculated from the Crust 2.0 model, ETOPO1 and ocean cooling model. Tensional deviatoric stresses are shown by red arrows while compressional deviatoric stresses are shown by black arrows. Length of the arrows are proportional to the magnitude of vertically integrated stresses. Strike-slip regions are indicated by one tensional and one compressional pair of arrows. High GPE areas are in deviatoric tension while low GPE areas are in deviatoric compression.

through compensation of the Crust 2.0 model via elevation adjustment. This is difficult to achieve, mainly because of differences in resolution between the convection and the Crust 2.0 models. Moreover, the prediction of radial tractions in the convection models are not necessarily compatible with observations and strongly depend on the assumption of whole mantle versus layered mantle convection [*Wen and Anderson*, 1997c]. Hence, although we have experimented with both methods, we prefer the first method, avoiding the controversy in predicting radial tractions in convection models. In this first method, employed in this paper, the contribution of radial tractions is assumed to be embedded in the total depth integral of σ_{rr}, from surface topography to reference level, r_L.

2.5. Deriving Absolute Viscosity, Strain Rate, and Velocity Through a Postprocessing Step

[20] The finite element (FE) model also generates strain rates and velocities. Although the predicted deviatoric stresses depend only on the effective body forces (driving forces) and the relative viscosity distribution, the magnitudes of the predicted strain rates and velocities depend on absolute values of the viscosities. The relative values of strain rates and velocities are already defined within the model solution. The absolute values of these (viscosities, strain rates, and velocities) is obtained in a postprocessing step, which has no impact on the stress solution. We first place our global velocity field in a kinematic no-net-rotation (NNR) frame through the requirement that it satisfies $\int (v \times r)\mathrm{d}S = 0$, where v is the horizontal surface velocity at position r and S is the area over the Earth's surface. Note that all motions were initially determined relative to a small rigid spherical cap in the center of Antarctica (–87.5 to –90 latitude). The transformation into an NNR frame simply involves finding the single rigid body rotation to the entire global velocity field that satisfies the NNR constraint in the equation above. We then find the single scaling factor of the entire relative global viscosity field (which before scaling varied between values of 1.0 for the plates to values as low as 10^{-3} for rapidly straining regions) that minimizes the misfit of the dynamic velocity field, in an NNR frame, with the kinematic NNR velocity field of *Kreemer et al.* [2006], defined by GPS observations. The one single scaling factor therefore defines the absolute values for the global viscosity field, strain rate field, and velocity field. The best fit to this kinematic model is obtained when an absolute viscosity of 10^{23} Pa-s is chosen for the plates [*Ghosh and Holt*, 2012].

3. Deviatoric Stresses Due to GPE Differences

[21] We use the Crust 2.0 model to calculate GPE (Figure 1). We calculate the depth integral of σ_{rr} down to a constant reference level, r_L (in equation (7)), which is taken as 100 km below sea level. A fixed mantle density of 3238 kg/m^3 is assumed from the crustal base to the depth r_L. The cooling plate model based on ocean floor age data [*Müller et al.*, 2008] with revised parameters from *Stein and Stein* [1992] is used to define densities for oceanic mantle regions. The Crust 2.0 model is not compensated (unequal pressure at the reference level r_L), and we assume that depth integrals of σ_{rr} down to reference level r_L already contain the contribution from the radial tractions

responsible for dynamic topography. Elevated regions have high GPE. Areas such as old ocean floors, trenches, and areas with thick sediment cover such as off the coast of eastern India and Africa and Gulf of Mexico, have low GPE. The deviatoric stress field from GPE differences (Figure 1) shows deviatoric tension in areas such as Andes, western North America, eastern Africa, Tibetan plateau, and the mid-oceanic ridges, whereas areas with low GPE show deviatoric compression. The Tibetan plateau shows large N-S deviatoric tension (principal axes with values of $\sim 3 \times 10^{12}$ N/m), associated with large GPE contrasts with the surrounding regions. We will later show that this N-S component of deviatoric tension is cancelled out by a compressive stress associated with basal tractions, generated by large scale density buoyancy-driven mantle circulation.

4. Deviatoric Stresses Due to Mantle Buoyancies

4.1. Lateral Viscosity Variations in the Convection Models

[22] In a previous paper, we have discussed the sensitivity of different radially symmetric viscosity models in influencing the lithospheric stress field [*Ghosh et al.*, 2008]. Since one of the goals of the present paper is to predict plate motions as well, and since lateral viscosity variations are necessary to generate plate motions, we restrict our discussion to models of laterally variable viscosity structures only.

[23] We introduce lateral viscosity variations in our convection models on the basis of major geological features. The presence of weak plate boundaries has been argued to be a major cause of viscosity differences within the lithosphere [*King and Hager*, 1990; *Zhong and Gurnis*, 1995a, 1995b]. We introduce weak zones by assuming that the plate boundary zones have a viscosity that is inversely proportional to strain rates from *Kreemer et al.* [2003] and *Ghosh et al.* [2009]. This is a reasonable assumption, although it does not give insight about the process by which plate boundary zones evolve to possess such strain rate dependent weakness (equation 8). The cold roots of continental cratons are also thought to be one of the principal causes of lateral viscosity variations in the shallow mantle. These high seismic velocity areas, seen in seismic tomography images, have been attributed to a chemically different composition, having a much higher viscosity than the surrounding mantle at the same depth [*Jordan*, 1978, 1988; *Rudnick and Nyblade*, 1999]. Age differences in the oceanic lithosphere can also be a major factor in giving rise to lateral viscosity differences. As the thickness of the oceanic lithosphere varies with age, the mantle close to the ridges can be expected to be weaker than that under old oceans. We consider these first order features to introduce lateral viscosity variations in both the lithosphere and the asthenosphere of the convection models. The lower mantle is assigned a viscosity 10 times higher than the upper mantle. The lateral changes in viscosity are confined within the top 200 km, implying that our models do not include viscosity variations due to slabs, which have been considered in some other dynamic modeling studies [cf. *Alisic et al.*, 2012]. Since controversies abound regarding the true strength of slabs [*Zhong and Gurnis*, 1995a; *Moresi and Gurnis*, 1996; *Zhong and Davies*, 1999; *Enns et al.*, 2005; *Stegman et al.*, 2006; *Billen*, 2008; *Liu and Stegman*, 2011], we have decided not to address this issue in the present study. The viscosity changes due to weak zones, as well as due to strength differences between old and young oceans, are confined within the lithosphere (top 100 km), whereas the viscosity changes arising due to cratonic keels are extended to depths below 100 km.

[24] For each viscosity structure, we generate deviatoric stresses computed via the method described in sections 2 and 3 and compare them with GSRM strain rate tensors as well as with $SH_{\max}$ directions from WSM. In addition to predicting stresses, we compute surface plate motions as described in section 2.5. We also compute the poloidal and toroidal components of velocity and expand them in spherical harmonics up to degree and order 20. We compute correlation between the kinematic and dynamic models for each degree and sum them up to obtain a total correlation, each for the poloidal (P/P') and toroidal components (T/T') (Table 1). The power at each degree for the poloidal and toroidal components are also computed and the ratio of toroidal/poloidal power (T/P) are calculated and compared with the T/P ratio from the kinematic model. Based on the match with the deformation indicators and plate motions, we delineate a range of viscosity models that satisfy both these constraints.

4.2. Generation of Toroidal Flow

[25] As mentioned earlier, the convective flow of the Earth has a toroidal component in addition to a poloidal one, which is responsible for the strike-slip motion along transform fault boundaries. The generation of this toroidal motion is, however, somewhat enigmatic. An incompressible Boussinesq fluid can only give rise to a toroidal flow field in the presence of lateral viscosity variations. Moreover, it has been shown by [*Hager and O'Connell*, 1979] that there occurs an equipartitioning of the Earth's poloidal and toroidal energy at each degree of spherical harmonic expansion. Toroidal flow cannot arise in two-dimensional models of mantle convection and hence only 3-D models of mantle convection can attempt to generate toroidal flow.

[26] In the past, a number of studies have attempted to generate toroidal motions in 3-D models of mantle convection. *Ricard and Vigny* [1989] created toroidal flow in their Cartesian model by imposing plate geometries as well as by determining plate motions through a torque balance method. *Gable et al.* [1991] also generated toroidal motion by imposing a hybrid stress and velocity boundary conditions in their models of spherical geometry. Both studies ignored lateral viscosity variations. The first study to generate toroidal flow in a dynamically self-consistent way was by *Christensen and Harder* [1991]. However, because of small lateral viscosity variations in their model, they were able to generate only a very small percentage of the observed toroidal velocity. *Ribe* [1992] included lateral viscosity variations in the lithosphere of his thin viscous shell and was able to give rise to a substantial toroidal flow field. *Bercovici* [1995], on the other hand, employed special rheology in order to generate sufficient toroidal flow. *Zhang and Christensen* [1993] used a temperature-dependent Newtonian viscosity model, as well as strain rate dependent non-Newtonian model, to generate toroidal motion in a dynamically self-consistent way. However, they failed to achieve the required toroidal/poloidal partitioning ratio. *Wen and Anderson* [1997b] generated toroidal motion self-consistently in their convection model by taking into account lateral viscosity variations in the lithosphere between continents and oceans. They found that a

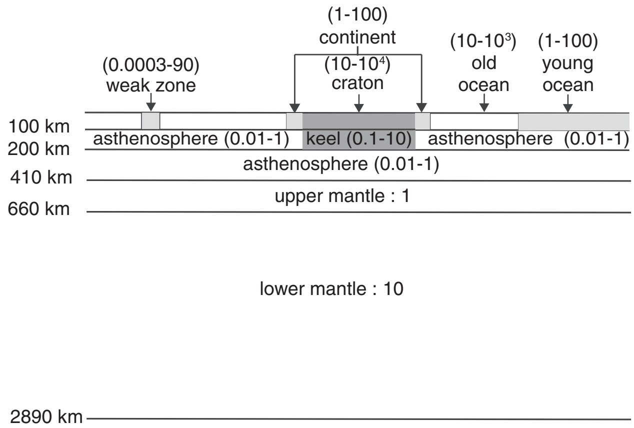

Figure 2. Viscosity structure of the convection models. The range of viscosities, relative to the reference viscosity of 10^{21} Pa-s, that are tested, are shown above or beside each type of feature. For example, the continental viscosities in our models range from 1 to 100 times the reference viscosity, that is, $10^{21} - 10^{23}$ Pa-s, whereas the cratons range in viscosities from $10^{22} - 10^{25}$ Pa-s.

relative lateral viscosity difference of a factor of 30, along with a weak asthenosphere, were able to generate a flow field that matched the observed toroidal/poloidal ratio as well as the observed plate motions. In the following section, we discuss the various types of viscosity structures and explore which models yield a good match to both the plate motion and deformation indicator data.

5. The Viscosity Models

[27] Lateral viscosity variations are introduced in three ways. The ocean floor age data of *Müller et al.* [2008] is used to introduce lateral viscosity variations in the lithosphere; oceans older than 70 Myr are assigned higher viscosities (1–3 orders of magnitude) than younger oceans (Figure 2). The second way is to introduce strong cratons within the continents using the keel model of *Wen and Anderson* [1997a]. In some models the cratons are allowed to reach into the asthenosphere up to a depth of 200 km, whereas in some they are restricted to the lithosphere. That is, we introduce lateral viscosity variations in both the lithosphere and within asthenosphere equivalent depths. The strength of the cratons in the lithosphere vary between 1–4 orders of magnitude higher than reference upper mantle viscosity whereas in the asthenosphere the keels range in stiffness between 0.1 to 10 times the reference viscosity, depending on the ambient asthenosphere viscosity. Higher viscosity keels at asthenosphere depths could not be tested due to convergence issues arising from such strong lateral variations. The third way in which we generate lateral viscosity variations is by taking into account weak zones. In a few models we restrict the weakness to plate boundaries alone; in others the continental deformation zones are also included. The viscosities of the weak zones in the convection model are based on the strength of the weak zones in the lithosphere model (discussed in section 2.1, equation (8)). The thickness of the asthenosphere is 300 km and its viscosity is varied between 1 and 2 orders of magnitude lower than reference viscosity (Figure 2).

[28] As mentioned earlier, plate velocities and deviatoric stresses predicted by the convection models are added to the predictions from GPE differences and the combined results are presented in Table 1. The global RMS misfit between the combined plate velocities and plate velocities from *Kreemer et al.* [2006] is calculated and presented in Table 1 under "RMS". The poloidal and toroidal components of plate velocities are computed and expanded up to spherical harmonic degree 20. A correlation coefficient for each degree and order between the modeled poloidal, toroidal components, and those from *Kreemer et al.* [2006] are calculated and the average of that correlation is presented in the table (P/P' and T/T'). A simple arithmetic mean underestimates the population correlation as the distribution of coefficients becomes negatively skewed when they are greater than zero [*Silver and Dunlap*, 1987]. Hence, we have used Fischer's z-transformation [*Fisher*, 1921] to transform the correlation coefficients (r) to z values before averaging them. In the next step we transform the averaged z's back to r. The models that yield a correlation coefficient of greater than 0.80 with the stress indicators and that which produce an RMS misfit of less than 10.2 mm/yr for plate motions as well as correlation coefficients of 0.90 and above for both the average poloidal and toroidal components are considered as successful models. The toroidal-poloidal velocity ratio is also inspected to ensure that they are close enough to the observed kinematic ratio.

[29] We test each of the lateral viscosity case separately as well as in combination with each other. Various paired combinations of the above viscosity structures are tested against the constraints of strain rate tensor information, RMS misfit to surface plate motions, and toroidal-poloidal pattern and velocity ratio. Table 1 lists majority of the lateral viscosity models that we experimented with as well as the results of quantitative analysis with stress indicators and plate motions. The maximum global average correlation coefficient between the modeled deviatoric stresses and the strain rate tensors achieved by these models is 0.85 ($\pm$ 0.02 at 95% confidence) and the lowest RMS misfit with surface plate velocities is 10.1 mm/yr. The z-values obtained from the correlation coefficients satisfy a Gaussian distribution, where half of the 8588 areas possess a correlation coefficient of 0.85 or greater for the optimal models. The models simultaneously showing a correlation of 0.85 and an RMS misfit of 10.1 mm/yr are considered to be the most successful. These are the models 7, 8, 18, 31, 37, 45, 47, and 48. Not surprisingly, these models also show the highest correlation with the observed poloidal and toroidal components of plate motions. We have conducted Z-tests to ensure that the correlation coefficients are

Table 2. Toroidal-Poloidal Velocity Ratio From the Kinematic Velocity Model [*Kreemer et al.*, 2006] and the Best-Fitting Dynamic Model (Model 47) for Spherical Harmonic Degrees 2–20

Degree	2	3	4	5	6	7	8	9	10	11	12	13	14	15	16	17	18	19	20
Kinematic	1.25	1.95	0.56	1.38	0.57	0.83	1.57	0.94	1.27	0.85	0.63	1.02	1.25	0.77	0.92	0.68	1.22	1.69	1.51
Dynamic	1.01	1.90	0.32	0.92	0.32	0.56	1.50	0.69	0.79	0.80	0.48	0.76	1.15	0.67	0.72	0.51	0.87	0.98	1.46

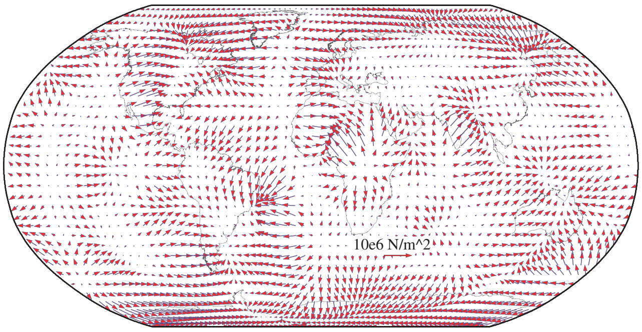

Figure 3. Global distribution of horizontal tractions, $-\tau_{r\varphi}$, $\tau_{r\theta}$, at the reference level r_L (100 km depth) based on a convection model with laterally variable viscosity structure in the lithosphere and asthenosphere (model 47 in Table 1).

significantly different. For example, models with a value of 0.82 are statistically different from those with 0.85 at both the 95% and 99% confidence levels. The general trend that emerges from the examination of the successful models is that all of them have (1) a stiff lithosphere (10^{23} Pa-s), (2) a moderately weak asthenosphere (10^{20} Pa-s), (3) either mild (1 order of magnitude) or no lateral viscosity variations in the asthenosphere between depth of 100–200 km, and (4) at least 3 orders of magnitude of lateral viscosity variations in the lithosphere produced by either stiff cratons or high viscosity areas of old oceanic regions or both. Presence or absence of weak zones in the convection model do not seem to make any significant difference as models with (37, 45, 47, 48) or without (7, 8, 18, 31) weak zones are able to match the deformation indicators and plate motions equally well. This could potentially be due to the lower resolution (degree 31) of the convection models. It should however be noted that the FE lithosphere model takes into account these weak zones within plate boundaries and they play a very important role in determining the style of stresses [*Ghosh et al.*, 2009].

[30] We had shown earlier [*Ghosh et al.*, 2008] with simpler flow models that had only radial strength variations that a large viscosity contrast between the lithosphere and the asthenosphere is necessary in order to achieve a good fit to the deformation indicators. This seems to be true for models that contain lateral viscosity variations as well. All models with lithosphere weaker than 10^{23} Pa-s fared poorly when compared to the strain rate tensors (Table 1) with correlation less than 0.8 and the cases with lithosphere of stiffness less than 10^{22} Pa-s show extremely poor correlation (16, 21–24, 28–29). As for comparison with plate motions, most of the less strong lithosphere cases show poor correlation for the poloidal and toroidal components of velocity and a high RMS velocity misfit. A strong (10^{21} Pa-s) as well as a very weak (10^{19} Pa-s) asthenosphere fails to match deformation indicators (1, 4, 11, 15-17, 19, 21, 24–26, 29, 35, 36, 43, 44), about half of them also failing to fit plate motions (1, 11, 21, 24, 29). Also, having strong lateral variations in the asthenosphere degrades the fit to observations. Models with just 2 orders of variations at asthenosphere depths (100–200 km) do not fit surface velocities as well (1, 30, 46). Several models can be deemed successful; however, if we have to choose a single model, it would be model 47, which has up to 6 orders of magnitude of lateral viscosity variations in the lithosphere due to cratons, age differences in the oceans, and weak plate boundaries. It also has one order of lateral viscosity variations in the asthenosphere because of the presence of keels. It yields a combined correlation coefficient of 0.85 with the strain rate tensors, an RMS misfit of 10.1 mm/yr with global plate velocities, a correlation of 0.94 and 0.92 for the poloidal, toroidal components of plate motions, and a comparable toroidal/poloidal ratio with the observed (Table 2).

6. Deviatoric Stress Field and Plate Motions From the Successful Models

[31] All the models that yield a good fit to both the constraints of plate motions and deformation indicators display a similarity in the long-wavelength pattern of tractions ($\tau_{\varphi r}$, $\tau_{\theta r}$, equations (12) and (13), Figure 3), applied to the FE lithosphere model at 100 km. These models show greater flow velocities at depth compared to the reference level r_L in areas of downwelling flow, such as central Asia, the Southeast Asian subduction zone, South America, and eastern North America. The same depth dependence of flow velocity

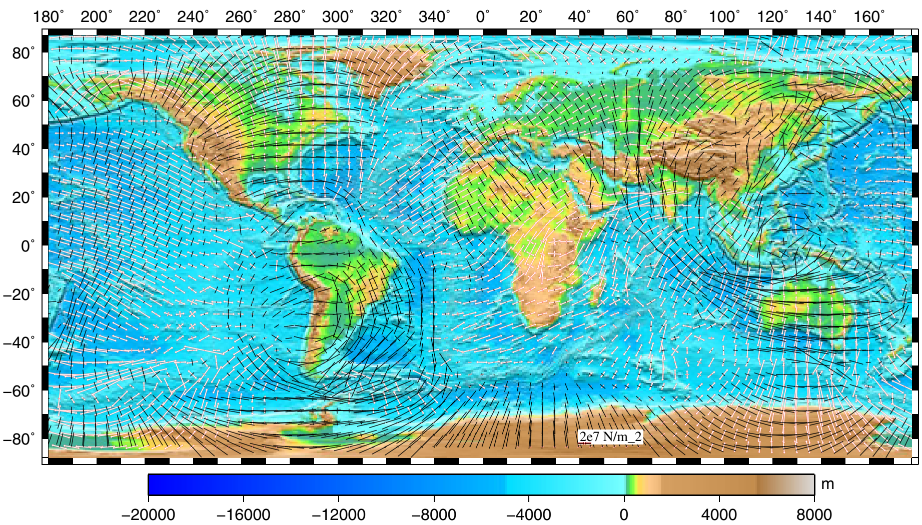

Figure 4. Global distribution of deviatoric stresses resulting from tractions in Figure 3.

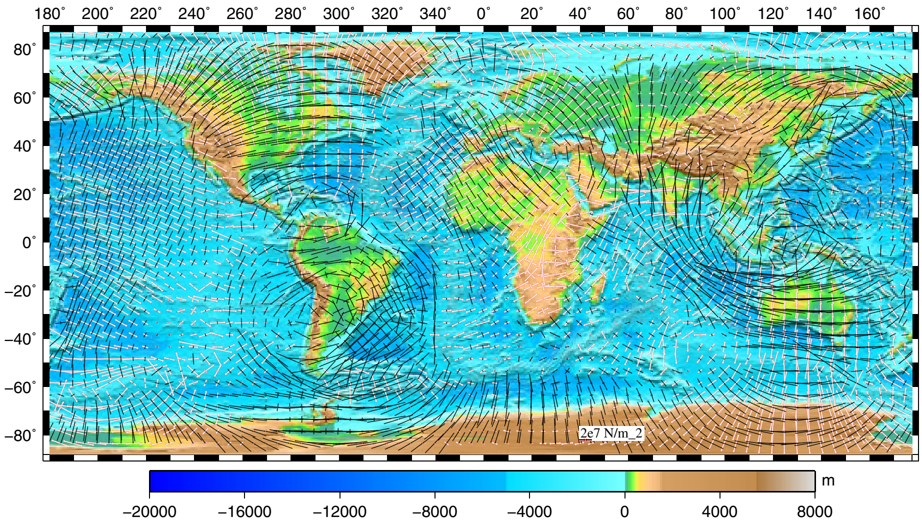

Figure 5. Combined deviatoric stresses from GPE differences (Figure 1) and basal tractions (Figure 4).

magnitudes applies to upwelling regions, such as East Africa and the Pacific. The flow velocity directions at greater depth will be in the direction of the traction associated forces shown in Figure 3. The traction magnitudes range from 5–10 MPa and their patterns hold a similarity with driving tractions for uniform thickness plates obtained by *van Summeren et al.* [2012]. The downwelling flow is caused by deeper density buoyancies of old subducted lithosphere. Similarity in the magnitude and distribution of tractions for all successful models also means similarity in the resultant deviatoric stress pattern (Figure 4). Hence, here we present the results of one of our successful models (model 47 in Table 1). The combined stress field, from GPE differences and basal tractions, (Figure 5) as well as the correlation coefficients with the strain rate tensor information (Figure 7), are also shown for this particular model. The viscosity model that generates the tangential tractions and plate motion predictions combines all the three features of weak plate boundaries, continental keels, and old versus young oceanic lithosphere. Table 3 lists the total correlation coefficients as well as the correlation coefficients averaged over certain regions, between the predicted deviatoric stress tensors and the GSRM strain rate tensors, from GPE contribution alone, basal tractions from model 47, and the combined GPE plus traction contribution. The combined case yields the best fit to the strain rate model. The GPE contribution seems to be playing a lesser role compared to the tractions (0.60 versus 0.84). The best-fit models favor a higher coupling to satisfy both the stress indicators and plate motions globally. However, this high average coupling poses problems locally for several regions of continental deformation, particularly western North America. This apparent need for heterogeneity of coupling, potentially resolved through the incorporation of smaller scale convection [e.g., *Faccenna and Becker*, 2010], is the next difficult problem to solve for global dynamic models.

Table 3. Correlation Coefficients, Averaged for a Particular Region, Obtained From a Comparison Between the Deviatoric Stress Tensors From GPE Differences, Tractions From One of Our Successful Models (Model 47 in Table 1), Combined GPE Plus Traction Model, and Strain Rate Tensors From the GSRM Model

Region of Interest	Number of Areas	GPE	Tractions	Combined GPE Differences Plus Basal Tractions
Western North America	618	0.46	0.81	0.78
Andes	440	–0.16	0.98	0.93
Eastern Africa	865	0.32	0.91	0.87
Mediterranean	352	0.68	0.59	0.75
Central Asia	995	0.25	0.62	0.61
Indo-Australian plate boundary zone	836	0.84	0.84	0.90
Mid-oceanic ridges	916	0.94	0.96	0.97
Western Pacific	538	0.42	0.87	0.84
Southeast Asia	800	0.59	0.77	0.82
Total	8588	0.60	0.84	0.85

[32] The magnitudes of principal axes of deviatoric stress from tractions, which range from 20–60 MPa, are somewhat larger than those from lithospheric GPE differences (10–40 MPa, Figure 1). The total depth integrated deviatoric stress field (Figure 5), which is the combined deviatoric stress field from lithospheric GPE differences (Figure 1) and mantle convection (Figure 4), shows significant changes from both Figures 1 and 4. For example, in Tibet, GPE differences predict deviatoric tension, whereas stresses from mantle tractions alone predict compression. However, the combined stresses show dominant strike-slip deformation in that area. The magnitudes of the second invariant of total deviatoric stresses range from 20–100 MPa for most areas (Figure 6).

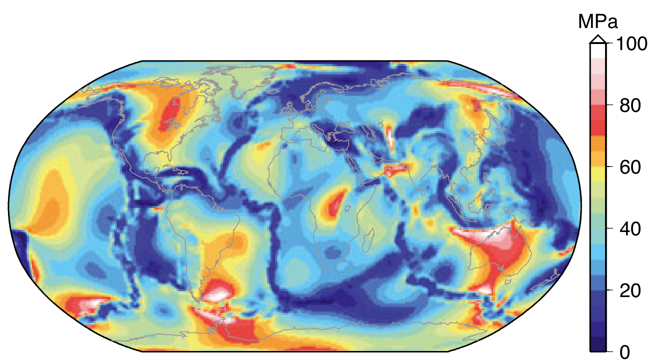

Figure 6. Second invariant of deviatoric stresses from our best-fitting dynamic model. Figure from supplementary section of *Ghosh and Holt* [2012].

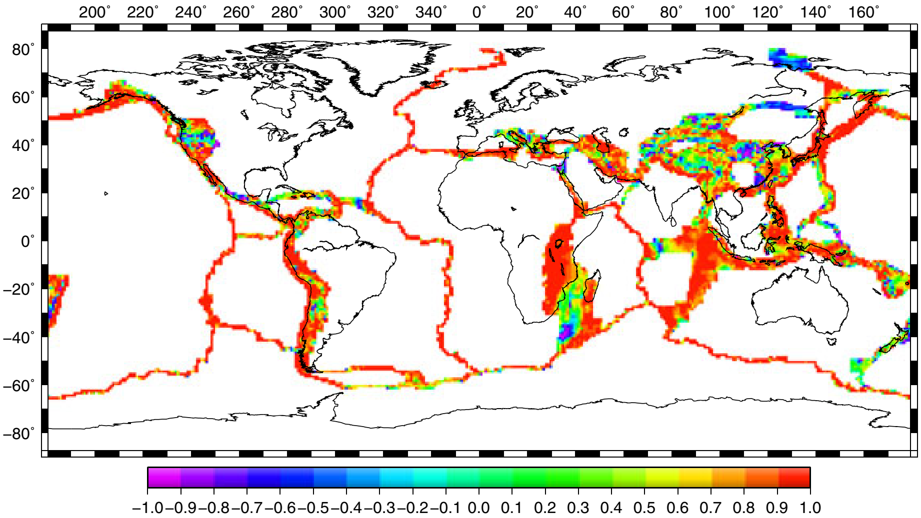

Figure 7. Correlation coefficients between deviatoric stress tensors arising from combined GPE differences and basal tractions (Figure 5) and observed strain rate tensors from the Global Strain Rate Map. Figure from supplementary section of *Ghosh and Holt* [2012].

[33] The deviatoric stress tensors from the combined influence of lithospheric GPE and mantle circulation (Figure 5) shows an improvement in fitting the strain rate tensors in the plate boundary zones compared to stresses from mantle circulation only. The improvement occurs in most areas, especially in areas of continental deformation (Table 3 and Figure 7). Areas such as the Andes, continental Africa, Indo-Australian plate boundary zone, eastern Asia, and the mid-oceanic ridges show an excellent fit to the strain rate tensors. The fit, however, is poor in areas such as Baikal in Asia, New Zealand, and also in a few areas in western USA. The overall fit for the combined case is 0.85 for model 47 (Table 3), with a confidence interval of 0.84–0.86 at 95% significance level.

[34] We compare the most compressive principal axes directions and styles of our predicted deviatoric stresses from our best fitting combined model and the horizontal most compressive principal axes of stresses in the WSM [*Zoback*, 1992; *Reinecker et al.*, 2005]. WSM is a compilation of measured principal stress directions based on earthquake focal mechanisms, borehole breakout data and Quaternary fault slip directions. We use the WSM data interpolated on our $1^\circ \times 1^\circ$ grid (Figure 8a). This interpolated dataset is compared with the most compressive principal axes of deviatoric stress from GPE differences and tractions combined (from model 47, Figure 8b). A qualitative comparison shows large swathes of regions which demonstrate an excellent match. That is, in those areas, the difference in most compressive principal axes directions between our predicted stresses and those from WSM is less than 15° and the style of stresses also match. We also compute correlation coefficients between the combined deviatoric stresses from model 47 and the WSM stress tensors (Figure 8c). The style of stresses along the mid-ocean ridge (MOR) does not everywhere match the WSM $SH_{\max}$ styles, which display mostly strike-slip type of behavior in these regions. This arises mainly because of the dominance of some big strike-slip type earthquakes at the transform fault boundaries connecting ridge segments, and a relative paucity of moment release in normal fault earthquakes along the ridges themselves. The GSRM tensor field, on the other hand, possesses a dominant signal associated with the spreading process at the mid-oceanic ridges, in agreement with the dominant tension at the mid-oceanic ridges. The other notable misfit between the predicted stresses and the WSM occurs in many regions of the outer rise of the trenches, where normal faulting associated with slab bending occurs [*Stern*, 2002]. The methodology that we employ does not include flexural stresses, thereby explaining this systematic misfit along the outer rise regions.

[35] One of the goals of this study is to match stresses in complex orogenic zones. The principal deviatoric stresses (Figure 9a) and their corresponding $SH_{\max}$ axes (Figure 9b) in western North America shows opening of Basin & Range and strike-slip along the San Andreas fault. There is compression within the Juan de Fuca trench and the Cascadia forearc exhibits N-S compression. However, within the region of the Eastern Snake River Plain and Yellowstone, the extensional directions of deviatoric stresses are different from observed. This problem is associated with too much coupling with mantle flow in this model. The higher coupling produces too much compression across the Yellowstone region, the central Rockies and Colorado Plateau, thereby dominating the important signal from topography and lithosphere structure in these regions. We also examine the stress field in two other deformational areas, the central Mediterranean region (Figures 9c and 9f) and the India-Asia collision zone (Figures 9d and 9e). The predicted stresses in Tibet show a predominantly strike-slip style of deformation (also mixed with normal fault style deviatoric stress) and a rotation of $SH_{\max}$ within Tibet around the Eastern Himalayan Syntaxis region, similar to what is observed there (Figure 8a). This dominant strike-slip style of deformation is only obtained when mantle traction contribution is added to the contribution from GPE differences. The rotation of stresses within Eastern Tibet is mainly associated with contribution from shallow structure. In the Mediterranean region, the modeled stresses are compatible with findings of the deformation field there [*Kahle et al.*, 2000;

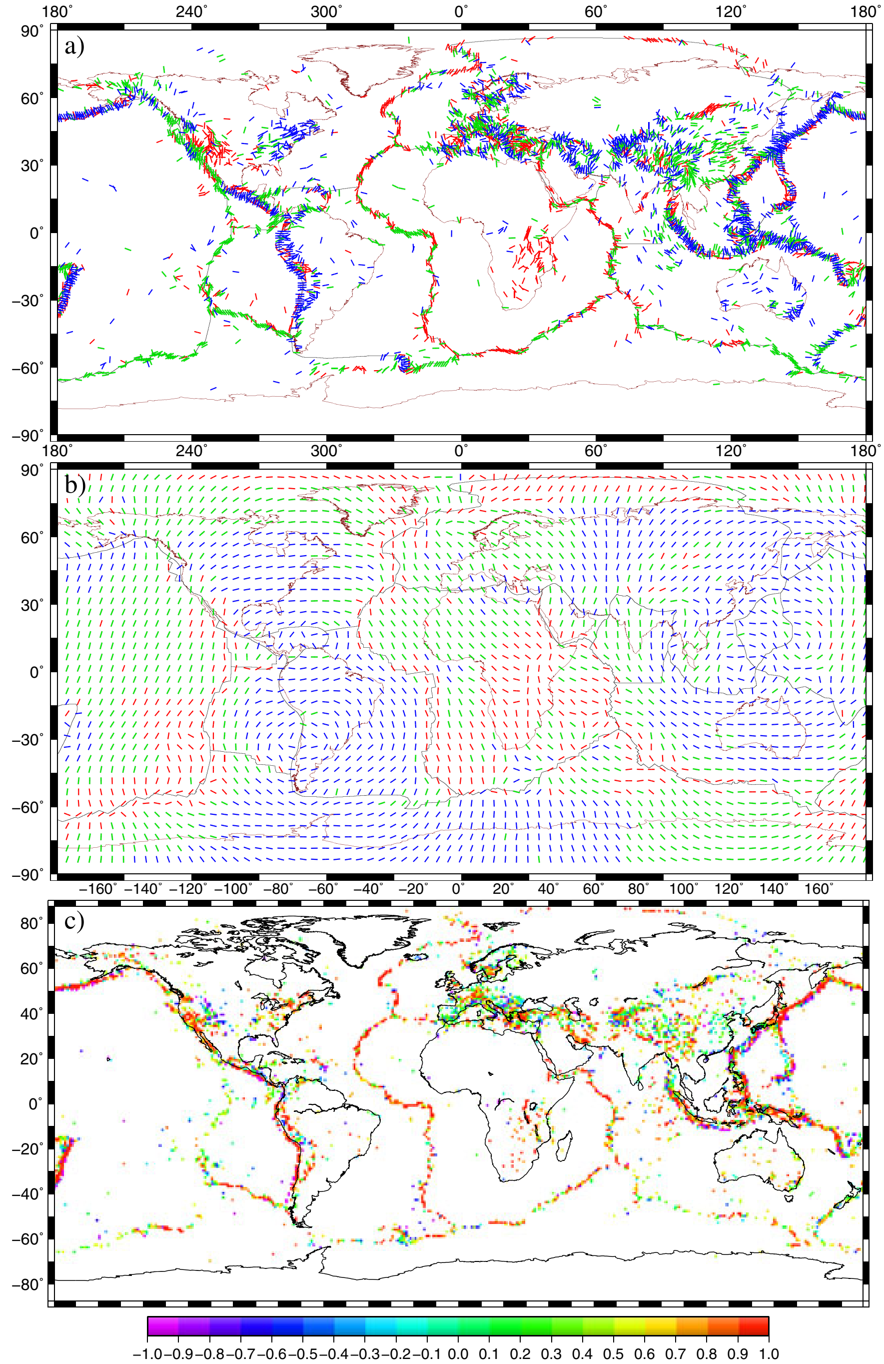

Figure 8. (a) SH_{max} directions (maximum horizontal stress orientations) from the World Stress Map averaged within $1^\circ \times 1^\circ$ areas. Red indicates normal fault regime, blue indicates thrust regime, whereas green denotes strike-slip regime. (b) Most compressive horizontal principal deviatoric stress axes from our best-fitting dynamic model (model 47). The colors indicate the strain environment predicted by the deviatoric stresses in the dynamic model. Red indicates the maximum horizontal compression orientation in a normal fault regime, blue indicates maximum horizontal compression in a thrust fault regime, and green denotes maximum horizontal compressive stress direction in a strike-slip regime. (c) Correlation coefficients between the predicted stress tensors from the above model and the WSM stresses. Modified from *Ghosh and Holt* [2012].

Jenny et al., 2004; *Kreemer and Chamot-Rooke*, 2004; *Ozeren and Holt*, 2010], although the global model presented here does not produce enough extension within the southern Aegean Sea region, which is almost certainly due to the fact that the mantle flow component used here is long wavelength and lacks the important effects of smaller scale convection in this region (slab roll-back) [*Faccenna and Becker*, 2010; *Faccenna et al.*, 2007]. Elsewhere the global model does an excellent job at predicting deformation within the Aegean and Eastern Turkey. The Hellenic arc shows trench-perpendicular compression whereas strike-slip deformation is seen along the North Anatolian fault.

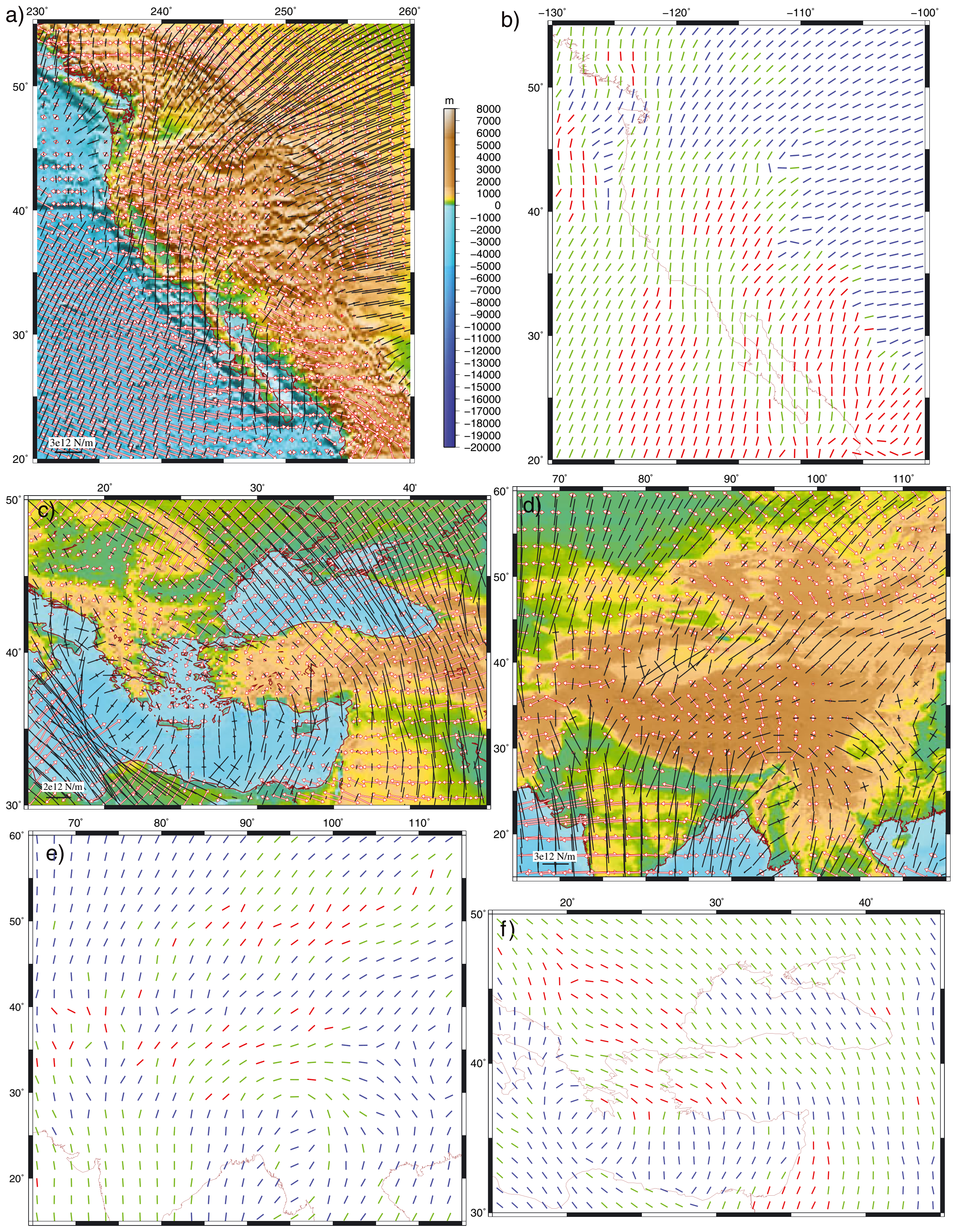

Figure 9. Deviatoric stress prediction from model 47 in the (a) western US, (c) central Mediterranean, and (d) India-Asia collision zone plotted on top of ETOPO1 topography. The most compressive principal axes of the stress tensors for the above regions are shown in Figures (b), (e), and (f). The color coding for Figures (b), (e), and (f) is the same as in Figure 8. Modified from *Ghosh and Holt* [2012].

[36] The surface plate velocities from our best-fitting model are presented here (red arrows in Figure 10) in an NNR frame along with velocities from the NNR kinematic model of *Kreemer et al*. [2006] (blue arrows). The modeled dynamic velocities match the kinematic velocities extremely well in most places. In Australia and in the southern Indian Ocean, the modeled velocities are offset from the kinematic by a few degrees. Also, we do not fit the motion of Cocos plate very well; we predict an easterly motion for the plate while the observed motion is northeasterly. The average

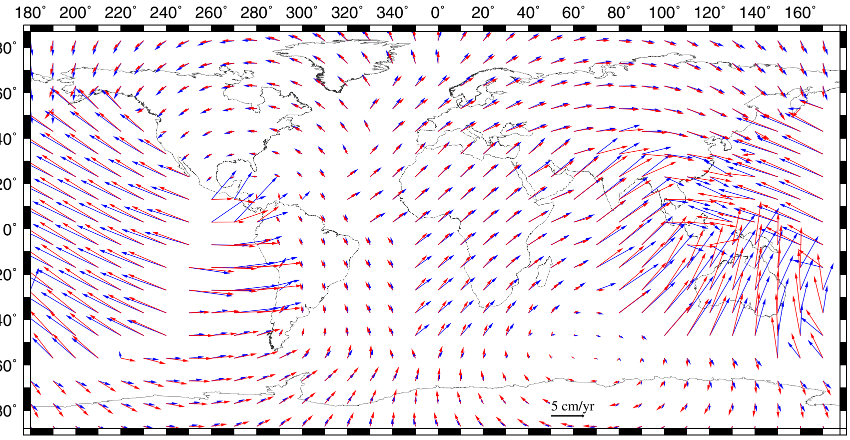

Figure 10. Kinematic no-net-rotation (NNR) model from *Kreemer et al.* [2006] (blue arrows) along with predicted velocities from our global dynamic model (red arrows) in an NNR frame. The dynamic model includes contributions from both coupling with whole mantle convection and from lithosphere structure and topography. Modified from *Ghosh and Holt* [2012].

global RMS misfit for this particular model with the kinematic NNR surface velocities is 10.1 mm/yr. We also calculate poles of rotation of major tectonic plates from our dynamic models (Table 4) (expanded from the seven plate results in *Ghosh and Holt* [2012]) and they are close to the rotation pole estimates from the latest NNR kinematic model, MORVEL [*Argus et al.*, 2011; *DeMets et al.*, 2010]. The North and the South American plates, Capricorn, Amurian plates show almost perfect fit to the poles of rotation. The predicted poles of Pacific, Europe, Nubia, Nazca, Somalia, and Arabia also lie fairly close to the observed locations.

[37] The strain rates predicted by our best fitting model (Figure 11) shows large swathes of nondeforming areas or low strain rates in the intraplate regions. Within the plate boundary zones, including a few continental deformation zones, strain rates are higher, between $50-5000 \times 10^{-9}$ yr^{-1}. These values are consistent with observations in the deforming areas of the Earth [*Kreemer et al.*, 2003]. The absolute viscosity values from our best fitting model, obtained by seeking a single scaling factor of the entire effective viscosity field that yields a best fit with the NNR surface motions of *Kreemer et al.* [2006], shows plates with values of 10^{23} Pa-s, with the weaker areas between 10^{19} and 10^{22} Pa-s (Figure 12) within the plate boundary zones.

7. Discussion and Conclusion

[38] In our earlier studies [*Ghosh et al.*, 2006, 2008], we had demonstrated how contribution from density driven mantle convection is necessary to predict the right style and orientation of stresses in many areas of the Earth, especially in continental deformation areas. However, the convection models that we had used were simpler with only radially variable viscosities and no lateral variations. In the present study we introduce lateral viscosity variations in the lithosphere and asthenosphere of our convection models to investigate the role of these in predicting the lithospheric stress field and plate velocities. An advantage of including lateral viscosity variations is it helps to delineate the nature of lithosphere-mantle coupling. Moreover, these lateral strength variations also enable us to include a second constraint, global plate motions, including toroidal-poloidal velocity ratio, in our quest of finding a best-fit coupling model.

Table 4. Angular Velocities of Major Plates as Predicted by Our Dynamic Model Compared With Kinematic Velocities From NNR-MORVEL [*DeMets et al.*, 2010; *Argus et al.*, 2011]

	Kinematic			Dynamic		
Plate	lon	lat	ω°/Myr	lon	lat	ω°/Myr
North America	–80.64	–4.85	0.209	–85.89	–1.31	0.141
South America	–112.83	–22.62	0.109	–112.22	–31.15	0.137
Europe	–106.50	48.85	0.223	–105.65	61.97	0.297
Nubia	–68.44	47.68	0.292	–90.10	45.29	0.236
Pacific	114.7	-63.58	0.651	106.84	–58.28	0.585
Nazca	–101.06	46.23	0.696	–96.01	59.97	0.633
Arabia	–8.49	48.88	0.559	13.58	51.06	0.597
Australia	37.94	33.86	0.632	49.13	10.86	0.599
Cocos	–124.31	26.93	1.198	–103.19	37.35	0.778
Somalia	–84.52	49.95	0.339	–106.02	42.803	0.340
India	–3.29	50.37	0.544	–51.75	48.00	0.522
Amuria	–122.82	63.17	0.297	–121.80	69.84	0.351
Philippine	–31.36	–46.02	0.910	–22.07	–71.22	0.547
Sunda	–95.02	50.06	0.337	–89.00	76.29	0.406
Capricorn	23.09	44.44	0.608	17.08	43.19	0.457
Antarctica	–118.11	65.42	0.250	–108.48	50.79	0.311

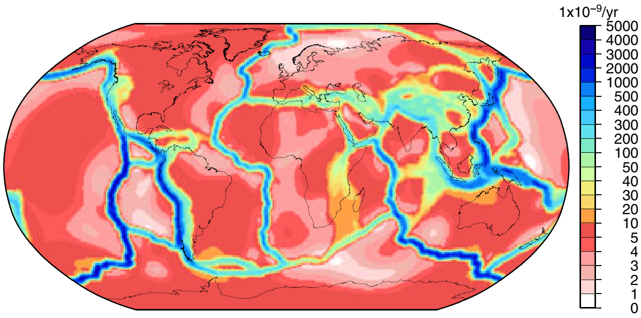

Figure 11. Strain rates predicted by model 47. The very small strain in the intraplate areas indicate that we are able to achieve rigid plates from our dynamic models. Figure from *Ghosh and Holt* [2012].

[39] Based on the numerous models that we experimented with, a stiff lithosphere (10^{23} Pa-s) is essential in matching deformation indicators as well as surface velocities. Our earlier study [*Ghosh et al.*, 2008] had argued for a large lithosphere-asthenosphere viscosity contrast on the basis of matching the deformation indicators only. *Ghosh et al.* [2010] had also showed the necessity of a stiff lithosphere based on fitting the Earth's long-wavelength geoid. The stiff lithosphere influences intraplate rigidity that is evident from the strain rates predicted by our best fitting model (Figure 11) where the intraplate areas are straining at very small rates, $1-4\times10^{-9}$/yr. The viscosity of the asthenosphere is also important in determining the best fitting model. Only a moderately weak asthenosphere (10^{20} Pa-s) is able to match the observational constraints. A stronger or a weaker coupling, produced using 10^{19} Pa-s and 10^{21} Pa-s, respectively, does not produce as good a fit. Many studies have argued for the existence of a low viscosity channel below the lithosphere. In fact, the plate motions predicted by *Wen and Anderson* [1997b] with a uniform low viscosity asthenosphere in their convection model, matched the observed plate motions quite well. This study has shown that such a viscosity model also does a very good job of matching the strain rate tensor information along the deforming plate boundary zones. Another important observation of this study is that the presence of lateral viscosity variations in the asthenosphere is not a necessary condition to match the surface observations. In fact, strong lateral variations in the asthenosphere degrade the fit to observations. Models with no or only weak (an order of magnitude) lateral variations in the asthenosphere give the best results. This has been argued earlier by *Naliboff et al.* [2009] by looking at stress magnitudes in the vicinity of continental keels. Also, all successful models have strong (at least 3 orders of magnitude) lateral viscosity variations in the lithosphere generated by stiff cratons and/or strong old ocean floor. A strong lateral viscosity contrast generates sufficient toroidal motion that satisfies the observed plate motions as well as near equipartitioning of toroidal-poloidal velocity ratio.

[40] An important aspect of our study is constraining deviatoric stress magnitudes in the lithosphere. The magnitudes of depth integrals of compressive deviatoric stress from the combined GPE differences and convection models are $3-7\times10^{12}$ N/m (30–70 MPa as a depth average), with the largest stresses occurring within the Indo-Australian plate region and southeast of South America in the Atlantic. The stress magnitudes in most parts are consistent with stress magnitudes of earlier studies [*Richardson*, 1992]. In other parts, our stress magnitudes are larger by a factor of 2. These areas of large stress magnitudes are outside the deforming plate boundary zones in the GSRM (Figure 6). Within the Australian plate, we predict peak compressive deviatoric stresses of about 7×10^{12} N/m (with second invariant of deviatoric stress approaching 100 MPa). However, within the Indo-Australian plate deforming zone, our predicted compressive deviatoric stresses range from $3-6\times10^{12}$, which are $\sim 25\,\%$ those of *Cloetingh and Wortel* [1986], who calculated stresses of 2–3 kilobars in the Indo-Australian plate boundary zone region. Our deviatoric stress solution within the Indo-Australian plate boundary zone is now consistent with stress magnitudes cited by *Molnar et al.* [1993], which they argued are sufficient to cause buckling and deformation of the Indian Ocean lithosphere. The higher magnitudes that we obtain in this study, in comparison with previous studies [*Ghosh et al.*, 2008, 2006], arise from the higher coupling with mantle flow, required to obtain a best-fit with global plate motions. However, *Coblentz et al.* [1998] predicted stress magnitudes smaller than ours in the Indo-Australian plate boundary region. Principal axes of deviatoric stresses at the Tibetan Plateau are between $2-3\times10^{12}$ N/m. The stress magnitudes of horizontal axes of compression in continental Europe are large, $\sim 5-6\times10^{12}$ N/m, whereas those in North America are between $4-6\times10^{12}$ N/m.

[41] Comparison of our predicted best fitting traction field with the surface velocities (Figures 3 and 10) indicates whether tractions are driving or resisting [*Ghosh and Holt*, 2012]. If mantle flow field is leading plate motion, tractions are driving, whereas they are resistive if mantle flow is trailing the plate. We devise a way of quantifying this driving versus resisting nature of tractions by computing the cosine of the differential angle between the traction and the velocity vectors at each point and multiplying them by the traction magnitudes weighted by the area (Figure 13). In areas like the Nazca plate, eastern North America, North Atlantic and western Europe, eastern Siberia, northeastern and northwestern Africa, Indian and Australian plates, and western part of the Pacific plate, the values are positive, indicating that tractions are driving in those regions. In these places both tractions and plate motions in an NNR frame act in similar directions and thus mantle flow is leading the plate motion. On the other hand, in areas such as western North America, the northern part of South America, and southern Africa, the values are negative. That is, tractions are resistive

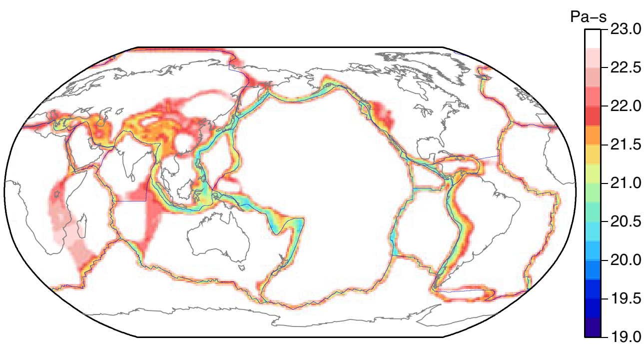

Figure 12. Absolute viscosities as given by model 47. The scale bar contains log of the viscosity values.

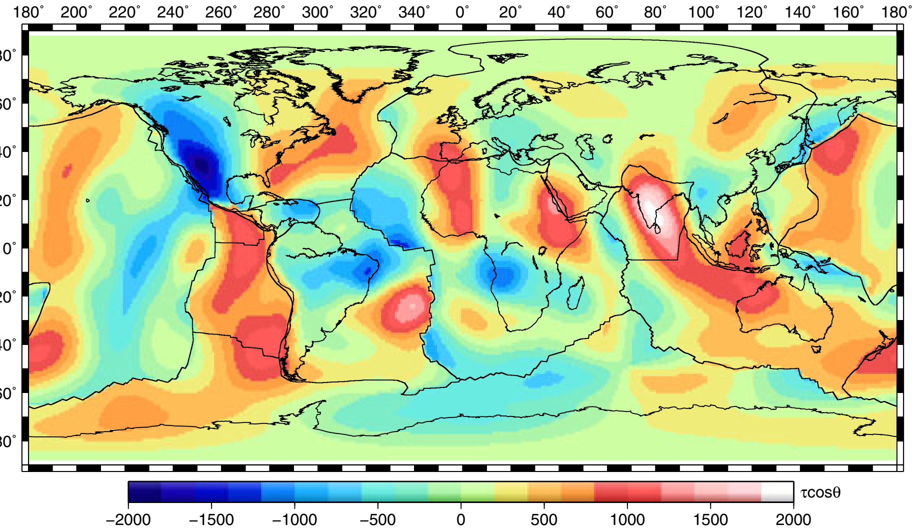

Figure 13. Plot of $\tau \times \cos\theta$ dA, where θ is the angular difference between tractions at the base of the lithosphere and surface velocity vectors in an NNR frame, τ are the traction magnitudes and dA are 1 x 1 degree areas, normalized by Earth's radius squared. This gives a quantitative indication of whether tractions are driving (positive) or resistive (negative). For example, at equatorial regions, a value of 2000 corresponds to a driving traction of about 6.5 MPa.

as plate motions are leading mantle flow. This observation addresses the controversy of whether mantle tractions are driving or resistive. Tractions are resistive within the vicinity of many oceanic ridge systems (Figure 13). Comparison of Figures 2 and 4, however, indicates the importance of tractions in producing extension along many of the ridge systems. The extensional influence of the tractions along the weak oceanic ridges in the Atlantic and much of the Indian Ridge is associated with large-scale flow patterns (Figure 3). These large-scale flow patterns reflect a primary influence of downwelling associated with subducted lithosphere (Farallon slab, subduction beneath South America, and subduction history beneath central and Southeast Asia). Such a large-scale flow pattern has been argued by *Becker and Faccenna* [2011] to be a major driving pattern for India and Arabian plates. That these tractions are resistive in places near the ridges indicates that, within these ridge-regions, the large-scale flow associated with the major downwellings dominates over any smaller-scale mantle flow involved with the sea-floor spreading process.

[42] We achieve the highest correlation coefficient of 0.85 between our predicted deviatoric stresses and the deformation indicators (Tables 1 and 3) and an RMS misfit of 1 cm/yr for surface motions. There still exists some misfit between our predictions and the observed plate motions and deformation indicators. The remaining misfit for the deviatoric stress field and the plate motions might arise from a number of different factors. For example, although our lithosphere model is a high resolution one (1×1 degree), the convection model is of much lower resolution (degree 31). The fit of the model to observations could certainly be improved by taking into account small-scale convection, which would require a higher resolution mantle convection model. There occurs substantial viscosity differences between the narrow weak plate boundaries and the more rigid plate interiors. These variations might play an important role. Although, our thin sheet lithosphere model takes into account these narrow weak zones, a degree 31 convection model may not be sufficient to handle these structures. In order to consider these weak, narrow plate boundaries, it is necessary to use a much higher resolution convection model. The model could also likely be improved through the use of a better structure model (within both the lithosphere and the mantle). However, this potential improvement is unlikely to change our conclusions about the relative role of shallow versus deeper sources and about the need for a dominance of driving tractions within many regions.

[43] One of the most important characteristics of the present study is joint prediction of stresses and plate motions in one self-consistent model. We have used both these constraints to delineate possible viscosity structures for the upper 200 km of the Earth. Second, we have incorporated the effects of topography and lithosphere structure, in addition to the contribution from mantle flow. We also quantify the relative contribution of these two driving forces, which is a controversial problem. We have shown that it is possible to fit both the observations of plate velocities and deformation indicators within the plates as well as in the plate boundary zones accurately, taking into account contribution from topography and lithosphere structure coupled with long-wavelength mantle tractions. Third, we have addressed the controversy regarding the relative contribution of driving versus resisting tractions and how this varies over the Earth's surface. Finally, our convection model is fully self-consistent with radial and lateral viscosity variations that are strong enough to generate sufficient toroidal motion. In order to fine-tune our models, additional constraints such as geoid and dynamic topography could be used. An accepted model would be one that is capable of matching all the four constraints of deviatoric stress field, plate motions, geoid, and topography.

Appendix A: Benchmarking

[44] We have shown earlier ([*Ghosh et al.*, 2008], online Supporting Information) that the thin sheet approximation is able to recover the depth integrals of deviatoric stresses in

the presence of large-scale three-dimensional flow for a case with only radial viscosity variations and no lateral variations, that is, a poloidal only case. This test demonstrated that our FE approach is correct and that while using the thin sheet approximation we are nevertheless able to recover horizontal stresses associated with dynamic topography and horizontal tractions associated with long-wavelength 3-D whole mantle convection. Here we demonstrate the suitability of the method in the presence of both poloidal and toroidal flow (both radial and lateral viscosity variations). We show this for a finer grid of $1° \times 1°$ whereas our prior experiment was on a coarser ($2.5° \times 2.5°$) grid. The sole purpose of this test is to check whether the vertically integrated deviatoric stresses from the thin sheet model can recover the deviatoric stresses from the 3-D convection model that possesses lateral viscosity variations. For this purpose we use an arbitrary lateral viscosity structure that has different strengths based on oceanic versus continental regions. The oceanic regions are assigned a viscosity of 10^{22} Pa-s whereas the continental regions are assigned a viscosity 30 times higher than that. The model has a weak (10^{19} Pa-s) asthenosphere up to 400 km, below which the upper mantle viscosity is constant at 10^{21} Pa-s with a 10 times stronger lower mantle. In the 3-D convection computation, the original $1° \times 1°$ viscosity structure is expanded into spherical harmonics degree. We use $l = 12$ here. The convective calculations yield both horizontal and radial tractions. Here we will show that the combined deviatoric stress field from the horizontal and radial tractions used as input into the FE model with thin sheet approximation matches the full 3-D stress field from the convection model in the presence of lateral viscosity variations. In order to prove this, we need to take the original lateral viscosity structure (described above) and expand it to $l = 12$ and use this viscosity structure as input in the FE thin sheet model (Figure A1).

[45] The horizontal tractions generated by the 3-D convection model at a depth of 100 km are applied at the base of the FE lithosphere model, and the deviatoric stresses are computed via the thin sheet method (Figure A2a). Next, the dynamic topography, predicted by the same convection model, is used to calculate depth integrals of σ_{rr}, or GPE, assuming PREM as the background density model. The resultant GPE variations are because of the presence of dynamic topography. From these GPE differences, deviatoric stresses are calculated via the thin sheet method (Figure A2b). Areas of positive dynamic topography (red and white) are in tension whereas those with negative dynamic topography (in blue) are in compression. It is to be noted that this stress field arises solely from the radial tractions (dynamic topography). In the next step, the stresses from horizontal tractions (Figure A2a) are added to those from radial tractions (Figure A2b) in order to obtain an estimate of the depth integral of the total stress field (Figure A3a).

[46] When the combined stress field obtained above is compared to the deviatoric stress field calculated directly from the full 3-D convection model (Figure A3b), we see an almost perfect match. For a quantitative comparison, we compute the correlation coefficients between the two deviatoric stress fields (Figure A4a). Most regions show a perfect correlation of 1. The differences that occur are in a few transitional areas, where stresses are very small. We also compute the ratio of the second invariants for the respective stress fields, $T1/T2$ (Figure A4b). Here T is given by $T = \sqrt{\tau_{\varphi\varphi}^2 + \tau_{\theta\theta}^2 + \tau_{rr}^2 + \tau_{\varphi\theta}^2} = \sqrt{2\tau_{\varphi\varphi}^2 + 2\tau_{\varphi\varphi}\tau_{\theta a} + 2\tau_{\theta\theta}^2 + 2\tau_{\varphi\theta}^2}$, where τ_{ij} are the deviatoric stresses. The correlation coefficient quantifies the quality of fit of the two stress fields in terms of direction and style, whereas the ratio of the second invariants gives a measure of fit in terms of magnitude for the two stress fields. For most of the surface areas, the stress

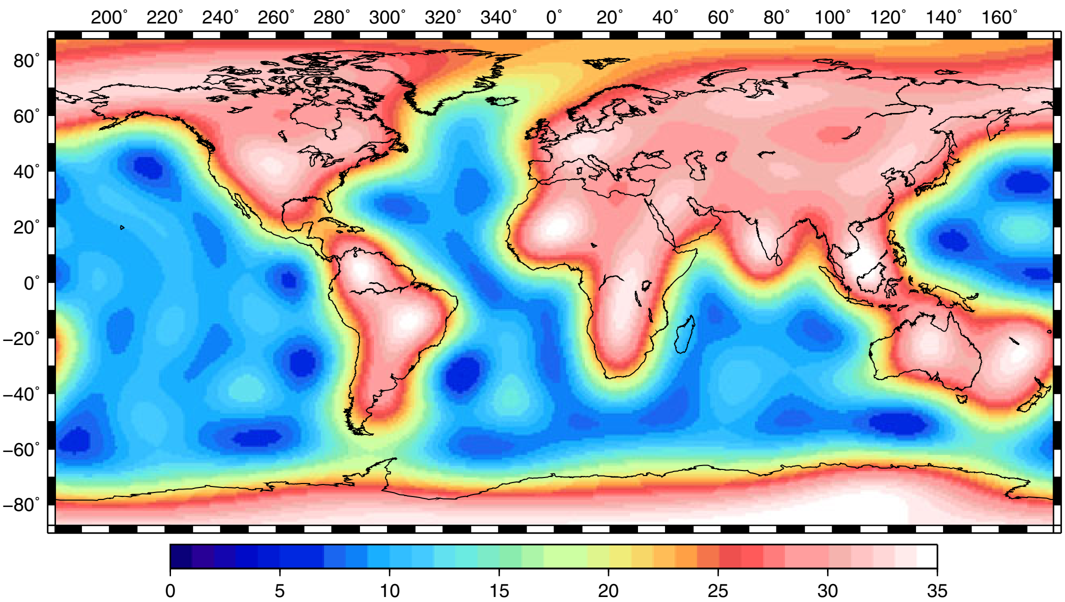

Figure A1. Lateral viscosity structure expanded into spherical harmonic degree 12 that is used as input viscosity in the thin sheet calculation for the benchmarking. The values are relative to a reference viscosity. The continents here have a higher viscosity than the oceanic regions.

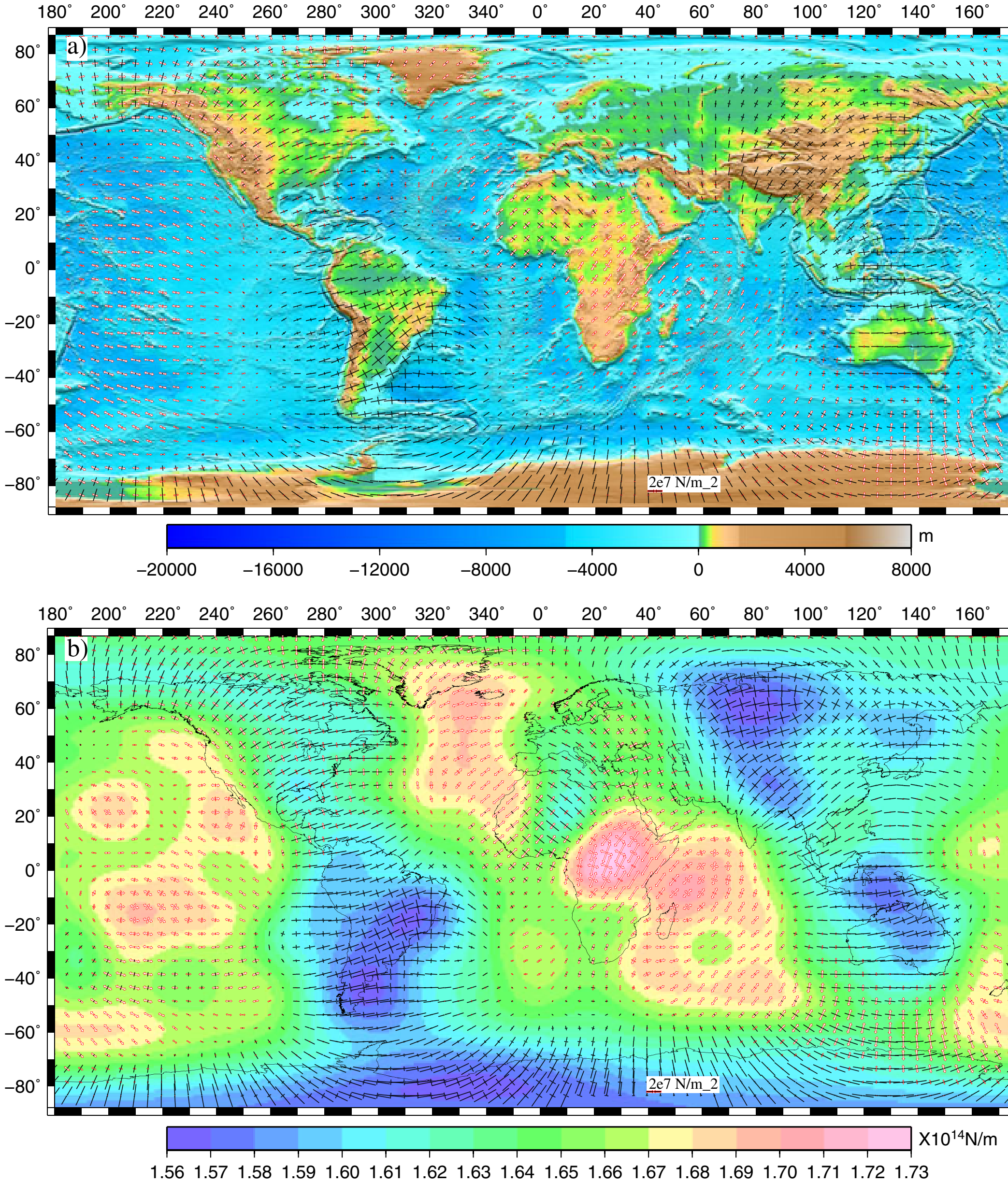

Figure A2. Deviatoric stress field computed via the thin sheet method from: (a) horizontal tractions generated by a 3-D convection model at 100 km depth, and applied to the base of the thin sheet, plotted on topography, and (b) radial tractions plotted on top of GPE (scale bar). The GPE is calculated from dynamic topography predicted by the 3-D convection model. The radial component of the 3-D mantle flow gives rise to the dynamic topography. These two solutions added together, define the total solution, which can be compared with the horizontal field from the 3-D mantle convection model.

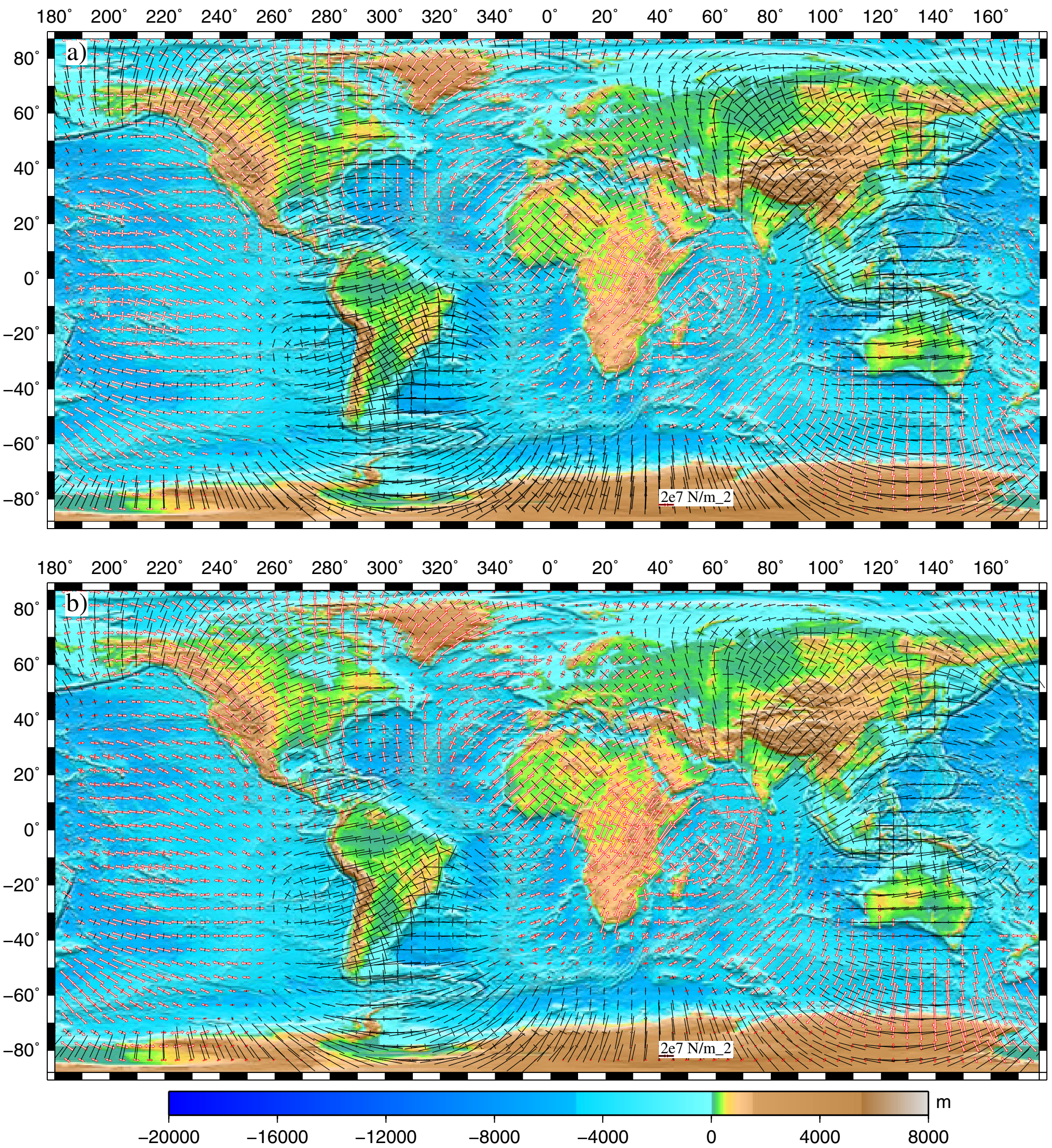

Figure A3. (a) Total deviatoric stress field obtained by adding stresses due to horizontal (Figure A2a) and radial (Figure A2b) tractions via the thin sheet method. (b) Deviatoric stress field obtained from the full 3D convection model. Note the similarity between Figures A2a and A2b.

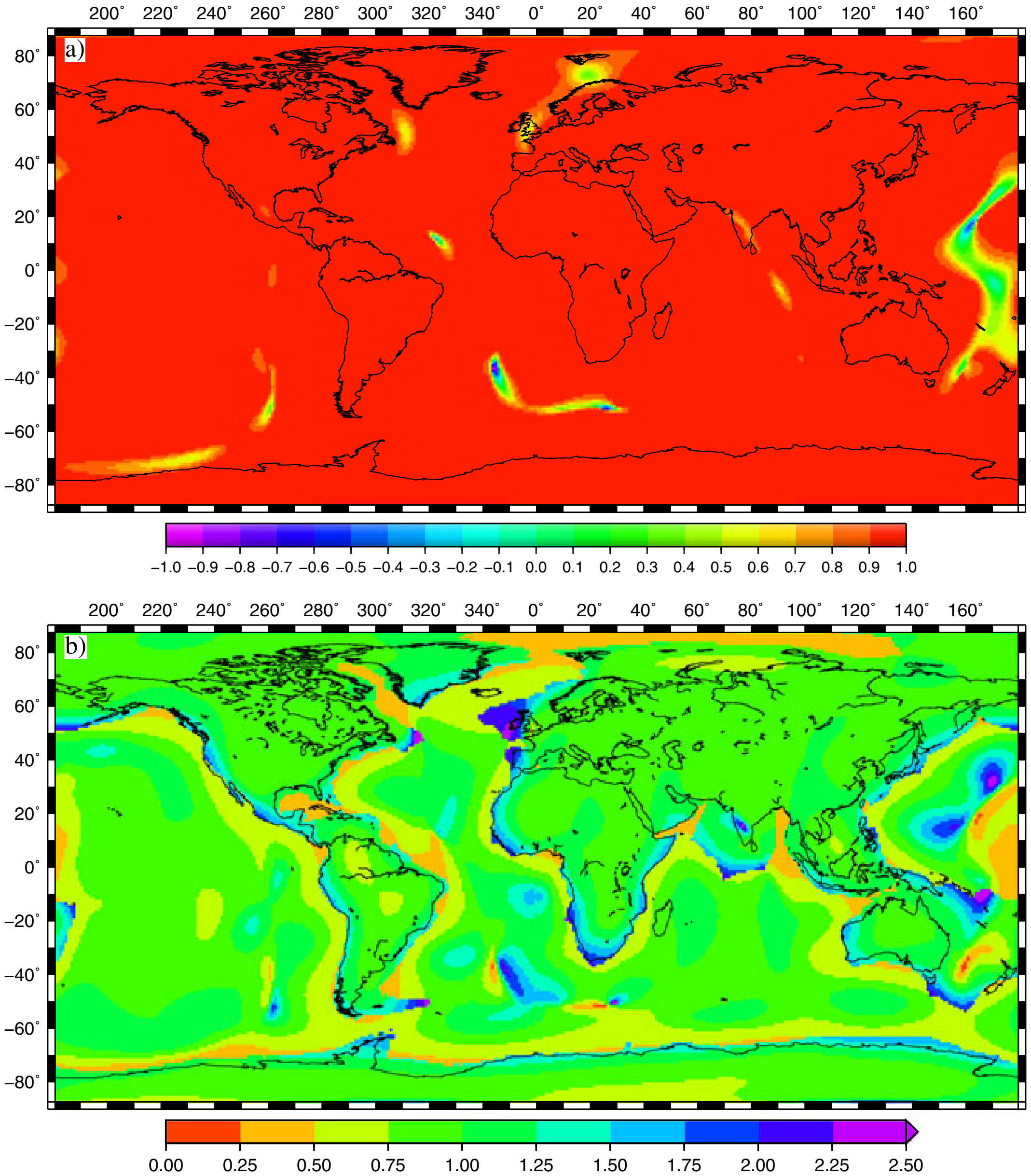

Figure A4. (a) Correlation coefficients between the two deviatoric stress fields in Figure A3. (b) Ratio, ***T*1/*T*2**, between the two deviatoric stress fields from Figure A3. *T*1 is the second invariant of deviatoric stress field output by the 3-D convection model (Figure A3b) and *T*2 is the second invariant of deviatoric stress field predicted by the thin sheet model (Figure A3a). In most areas the ratio is close to 1. In areas where it is not 1 normally correspond to the crossover areas, mentioned in text, where the deviatoric stresses are switching from tension to compression, and vice-versa. Also, the transitional areas where the changes from high viscosity to low viscosity occurs show ratios with ranges from 0.5 to 2.

magnitudes are a near-perfect match. Differences in magnitude arise near some areas with strong viscosity contrasts as well as within regions of transition where stresses are predicted to be very small. In these regions, differences in magnitude are around a factor of 2. In summary, we have shown that the thin sheet approximation method that we use has done a remarkably good job of recovering the styles stress field from a full 3-D convection model when lateral viscosity variations are present. In most regions the model recovers the correct stress magnitudes, with differences as high as a factor of 2 in some regions possessing strong viscosity contrasts.

[47] **Acknowledgments.** This work was supported by NSF Grants EAR-0310193, EAR-1214215 and EAR-0911300. We thank John Haines for his insights and help during the earlier phase of this project. We also thank two anonymous reviewers whose suggestions have improved the manuscript.

References

Alisic, L., M. Gurnis, G. Stadler, C. Burstedde, and O. Ghattas (2012), Multi-scale dynamics and rheology of mantle flow with plates, *J. Geophys. Res.*, *117*, B10402, doi:10.1029/2012JB009234.

Argus, D. F., R. G. Gordon, and C. DeMets (2011), Geologically current motion of 56 plates relative to the no-net-rotation reference frame, *Geochem. Geophys. Geosyst.*, *12*(Q11001), 13 pp., doi:10.1029/2011GC003751.

Artyushkov, E. V. (1973), Stresses in the lithosphere caused by crustal thickness inhomogeneities, *J. Geophys. Res.*, *78*, 7675–7690.

Bai, W., C. Vigny, Y. Ricard, and C. Froidevaux (1992), On the origin of deviatoric stresses in the lithosphere, *J. Geophys. Res.*, *97*, 11,729–11,737.

Becker, T. W., and C. Faccenna (2011), Mantle conveyor beneath the Tethyan collisional belt, *Earth Planet. Sci. Lett.*, *310*, 453–461.

Becker, T. W., and R. J. O'Connell (2001), Predicting plate velocities with mantle circulation models, *Geochem. Geophys. Geosyst.*, *2*, 171. 2001GC000.

Bercovici, D. (1995), A source-sink model of the generation of plate tectonics from non-newtonian mantle flow, *J. Geophys. Res.*, *100*, 2013–2030.

Bercovici, D. (1998), Generation of plate tectonics from lithosphere-mantle flow and void-volatile self-lubrication, *Earth Planet. Sci. Lett.*, *154*, 139–151.

Billen, M. (2008), Modeling the dynamics of subducting slabs, *Annu. Rev. Earth Planet. Sci.*, p. 10.1146/annurev.earth.36.031207.124129.

Bird, P. (1998), Testing hypotheses on plate-driving mechanisms with global lithosphere models including topography, thermal structure and faults, *J. Geophys. Res.*, *103*, 10,115–10,129.

Bird, P., Z. Liu, and W. K. Rucker (2008), Stresses that drive the plates from below: Definitions, computational path, model optimization, and error analysis, *J. Geophys. Res.*, *113*, B11406, doi:10.1029/2007JB005460.

Christensen, U., and H. Harder (1991), 3-d convection with variable viscosity, *Geophys. J. Int.*, *104*, 213–226.

Cloetingh, S., and R. Wortel (1986), Stress in the Indo-Australian plate, *Tectonophys.*, *132*, 49–67, doi:10.1016/0040–1951(86)90024–7.

Coblentz, D. D., R. M. Richardson, and M. Sandiford (1994), On the gravitational potential energy of the Earth's lithosphere, *Tectonophys.*, *13*, 929–945.

Coblentz, D. D., S. Zhou, R. R. Hillis, R. M. Richardson, and M. Sandiford (1998), Topography, boundary forces, and the Indo-Australian intraplate stress field, *J. Geophys. Res.*, *103*, 919–931, doi:10.1029/97JB02381.

DeMets, C., R. G. Gordon, and D. F. Argus (2010), Geologically current plate motions, *Geophys. J. Int.*, *181*, doi:10.1111/j.1365–246X.2009.04,491.x.

Enns, A., T. W. Becker, and H. Schmeling (2005), The dynamics of subduction and trench migration for viscosity stratification, *GJI*, *160*, 761–775.

Faccenna, C., and T. W. Becker (2010), Shaping mobile belts by small-scale convection, *Nature*, *465*, doi:10.1038/nature09,064.

Faccenna, C., F. Funiciello, L. Civetta, M. D'Antonio, M. Moroni, and C. Piromallo (2007), Slab disruption, mantle circulation, and the opening of the Tyrrhenian basins, *Geol. Soc America*, *418*, 10.1130/2007.2418(08) ed..

Fisher, R. A. (1921), On the probable error of a coefficient ofcorrelation deduced from a small sample, *Metron*, *1*, 3–32.

Fleitout, L. (1991), The sources of lithospheric tectonic stresses, *Roy. Soc. of London Phil. Trans.*, *337*, 73–81.

Fleitout, L., and C. Froidevoux (1982), Tectonics and topography for a lithosphere containing density heterogeneities, *Tectonophys.*, *1*, 21–56.

Fleitout, L., and C. Froidevoux (1983), Tectonic stresses in the lithosphere, *Tectonophys.*, *2*, 315–324.

Flesch, L. M., A. J. Haines, and W. E. Holt (2001), Dynamics of the India-Eurasia collision zone, *J. Geophys. Res.*, *106*, 16,435–16,460.

Forte, A., R. Moucha, N. Simmons, S. Grand, and J. Mitrovica (2010a), Deep-mantle contributions to the surface dynamics of the North American continent, *Tectonophys.*, *481*, 3–15.

Forte, A., S. Quéré, R. Moucha, N. A. Simmons, S. P. Grand, J. Mitrovica, and D. Rowley (2010b), Joint seismic–geodynamic-mineral physical modelling of african geodynamics: A reconciliation of deep-mantle convection with surface geophysical constraints, *Earth Planet. Sci. Lett.*, *295*, 329–341.

Forte, A. M., W. R. Peltier, A. M. Dziewonski, and R. L. Woodward (1993), Dynamic surface topography: a new interpretation based upon mantle flow models derived from seismic tomography, *Geophys. Res. Lett.*, *20*, 225–228.

Frank, F. C. (1972), Plate tectonics, the analogy with glacier flow, and isostasy, *Flow and Fracture of Rocks, Geophys. Monogr. Ser.*, *16*, 285–292, edited by H. C Heard et al., AGU, washington, D.C.

Gable, C. W., R. J. O'Connell, and B. J. Travis (1991), Convection in three dimensions with surface plates: generation of toroidal flow, *J. Geophys. Res.*, *96*, 8391–8405.

Ghosh, A., and W. E. Holt (2012), Plate motions and stresses from global dynamic models, *Science*, *335*, 838–843.

Ghosh, A., W. E. Holt, A. J. Haines, and L. M. Flesch (2006), Gravitational potential energy of the Tibetan Plateau and the forces driving the Indian plate, *Geology*, *34*, 321–324.

Ghosh, A., W. E. Holt, L. Wen, A. J. Haines, and L. M. Flesch (2008), Joint modeling of lithosphere and mantle dynamics elucidating lithosphere-mantle coupling, *Geophys. Res. Lett.*, *35*, L16309, doi:10.1029/2008GL034365.

Ghosh, A., W. E. Holt, and L. M. Flesch (2009), Contribution of gravitational potential energy differences to the global stress field, *Geophys. J. Int.*, *179*, 787–812.

Ghosh, A., T. W. Becker, and S. J. Zhong (2010), Effect of lateral viscosity variations on the geoid, *Geophys. Res. Lett.*, *37*, L01301, doi:10.1029/2009GL040426.

Hager, B. H. (1984), Subducted slabs and the geoid: Constraints on mantle rheology and flow, *J. Geophys. Res.*, *89*, 6003–6015.

Hager, B. H., and R. J. O'Connell (1979), Kinematic models of large-scale flow in the earth's mantle, *J. Geophys. Res.*, *84*, 1031–1048.

Hager, B. H., and R. J. O'Connell (1981), A simple global model of plate dynamics and mantle convection, *J. Geophys. Res.*, *86*, 4843–4867.

Hager, B. H., R. W. Clayton, M. A. Richards, R. P. Comer, and A. M. Dziewonski (1985), Lower mantle heterogeneity, dynamic topography and the geoid, *Nature*, *313*, 541–545.

Heidbach, O., M. Tingay, A. Barth, J. Reinecker, D. Kurfeb, and B. Müller (2008), The World Stress Map database release 2008, doi:10.1594/GFZ.WSM.Rel2008.

Jenny, S., S. Goes, D. Giardini, and H. G. Kahle (2004), Earthquake recurrence parameters from seismic and geodetic strain rates in the eastern mediterranean, *Geophys. J. Int.*, *157*, 1331–1347.

Jordan, T. H. (1978), Composition and development of the continental tectosphere, *Nature*, *274*, 544–548.

Jordan, T. H. (1988), Structure and formation of the continental tectosphere, *J. Petrology*, pp. 11–37, special lithosphere issue.

Kaban, M., I. Rogozhina, and V. Trubitsyn (2007), Importance of lateral viscosity variations in the whole mantle for modelling of the dynamic geoid and surface velocities, *J. Geodyn.*, *43*, 262–273.

Kahle, H. G., M. Cocard, Y. Peter, A. Geiger, R. Reilinger, A. Barka, and G. Veis (2000), GPS-derived strain rate field within the boundary zones of the Eurasian, African and Arabian plates, *J. Geophys. Res.*, *105*, 23,353–23,370.

Karpychev, M., and L. Fleitout (1996), Simple considerations on forces driving plate motion and on the plate-tectonic contribution to the long-wavelength geoid, *Geophys. J. Int.*, *127*, 268–282.

Kaula, W. M. (1975), Product-sum conversion of spherical harmonics with application to thermal convection, *J. Geophys. Res.*, *80*, 225–231.

King, S. D., and B. H. Hager (1990), The relationship between plate velocity and trench viscosity in newtonian and power-law subduction calculations, *Geophys. Res. Lett.*, *12*, 2409–2412.

Kreemer, C., and N. Chamot-Rooke (2004), Contemporary kinematics of the southern Aegean and the Mediterranean Ridge, *Geophys. J. Int.*, *157*, 1377–1392.

Kreemer, C., W. E. Holt, and A. J. Haines (2003), An integrated global model of present-day plate motions and plate boundary deformation, *Geophys. J. Int.*, *154*, 8–34.

Kreemer, C., D. A. Lavallee, G. Blewitt, and W. E. Holt (2006), On the stability of a geodetic no-net-rotation frame and its implication for the international terrestrial reference frame, *Geophys. Res. Lett.*, *33*, doi:10.1029/2006GL027,058.

Lithgow-Bertelloni, C., and J. H. Guynn (2004), Origin of the lithospheric stress field, *J. Geophys. Res.*, *109*, B01408, doi:10.1029/2003JB002467.

Liu, L., and D. R. Stegman (2011), Segmentation of the Farallon slab, *Earth Planet. Sci. Lett.*, *311*, 1–10. doi:10.1016/j.epsl.2011.09.027.

Molnar, P., P. C. England, and J. Martinod (1993), Mantle dynamics, uplift of the Tibetan plateau, and the Indian monsoon, *RG*, *31*, 357–396.

Moresi, L. N., and M. Gurnis (1996), Constraints on the lateral strength of slabs from three-dimensional dynamic flow models., *Earth Planet. Sci. Lett.*, *138*, 15–28.

Moucha, R., A. Forte, J. Mitrovica, and A. D. Daradich (2007), Lateral variations in mantle rheology: implications for convection related surface observables and inferred viscosity models, *Geophys. J. Int.*, *169*, 113–135.

Müller, R. D., W. Roest, J. Royer, L. Gahagan, and J. Sclater (1997), Digital isochrons of the world's ocean floor, *J. Geophys. Res.*, *102*, 3211–3214.

Müller, R. D., M. Sdrolias, C. Gaina, and W. R. Roest (2008), Age, spreading rates and spreading symmetry of the world's ocean crust, *Geochem. Geophys. Geosyst.*, *743*, 9, doi:10.1029/2007GC001

Naliboff, J. B., C. P. Conrad, and C. Lithgow-Bertelloni (2009), Modification of the lithospheric stress field by lateral variations in plate-mantle coupling, *Geophys. Res. Lett.*, *36*, L22307, doi:10.1029/2009GL040484.

Ozeren, S. M., and W. E. Holt (2010), The dynamics of the eastern Mediterranean and eastern Turkey, *Geophys. J. Int.*, *183*, doi:10.1111/j.1365–246X.2010.04,819.x.

Reinecker, J., O. Heidbach, M. Tingay, B. Sperner, and B. Müller (2005), The release 2005 of the World Stress Map, available online at www.world-stress-map.org

Ribe, N. M. (1992), The dynamics of thin shells with variable viscosity and the origin of toroidal flow in the mantle, *Geophys. J. Int.*, *110*, 537–552.

Ricard, Y., and C. Vigny (1989), Mantle dynamics with induced plate tectonics, *J. Geophys. Res.*, *94*, 5987–6002.

Richards, M. A., and B. H. Hager (1984), Geoid anomalies in a dynamic Earth, *J. Geophys. Res.*, *89*, 10, 299–10,313.

Richardson, R. M. (1992), Ridge forces, absolute plate motions, and the intraplate stress field, *J. Geophys. Res.*, *97*, 11,739–11,748.

Richardson, R. M., S. Solomon, and N. Sleep (1979), Tectonic stress in the plates, *Rev. Geophys.*, *17*, 981–1019.

Rudnick, R., and A. Nyblade, (1999), The composition and thickness of Archean continental roots: constraints from xenolith thermobarometry, in Mantle Petrology: Field Observations and High-Pressure Experimentation: A Tribute to Francis R. (Joe) Boyd, vol. *6*, edited by Y. Fei, C. Bertka, and B. Mysen, pp. 3–12, Geochemical Soc. Spec. Publ.

Sandiford, M., and D. Coblentz (1994), Plate-scale potential-energy distributions and the fragmentation of ageing plates, *Earth Planet. Sci. Lett.*, *126*, 143–159.

Silver, N. P., and W. P. Dunlap (1987), Averaging correlation coefficients: Should fischer's z transformation be used?, *J. Applied Psychology*, *72*, 146–148.

Solomon, S. C., N. H. Sleep, and R. M. Richardson (1975), On the forces driving plate tectonics: Inferences from absolute plate velocities and intraplate stress, *Geophys. J. R. Astron. Soc.*, *42*, 769–801.

Stegman, D., J. Freeman, W. Schellart, L. Moresi, and D. May (2006), Influence of trench width on subduction hinge retreat rates in 3-d models of slab rollback, *G3*, *7*, Q03012, doi:10.1029/2005GC001056.

Stein, C. A., and S. Stein (1992), A model for the global variation in oceanic depth and heat flow with lithospheric age, *Nature*, *1992*, 123–129.

Steinberger, B., H. Schmeling, and G. Marquart, (2001), Large-scale lithospheric stress field and topography induced by global mantle circulation, *Earth Planet. Sci. Lett.*, *186*, 75–91.

Stern, R. J. (2002), Subduction zones, *Rev. Geophys.*, *40*, doi:10.1029/2001RG000108.

Su, W. J., R. L. Woodward, and A. M. Dziewonski (1994), Degree 12 model of shear velocity heterogeneity in the mantle, *J. Geophys. Res.*, *99*, 6945–6980.

Tackley, P. (1998), Self-consistent generation of tectonic plates in theree dimensional mantle convection, *Earth Planet. Sci. Lett.*, *157*, 9–22.

Tackley, P. (2000), Mantle convection and plate tectonics: toward an integrated physical and chemical theory, *Science*, *288*, 2002–2007.

Thoraval, C., and M. A. Richards (1997), The geoid constraint in global geodynamics: Viscosity structure, mantle heterogeneity models, and boundary conditions, *Geophys. J. Int.*, *131*, 1–8.

Tosi, N., O. Cadek, Z. Martinec, D. A. Yuen, and G. Kaufmann (2009), Is the long-wavelength geoid sensitive to the presence of postperovskite above the core-mantle boundary?, *Geophys. Res. Lett.*, *36*, L05303, doi:10.1029/2008GL036,902.

Trompert, R., and U. Hansen (1998), Mantle convection simulations with rheologies that generate plate-like behaviour, *Nature*, *395*, 686–689.

van Summeren, J., C. P. Conrad, and C. Lithgow-Bertelloni (2012), The importance of slab pull and a global asthenosphere to plate motions, *Geochem. Geophys. Geosyst.*, *13*(1), Q0AK03, doi:10.1029/2011GC003873.

Wen, L., and D. L. Anderson (1997a), Slabs, hotspots, cratons and mantle convection revealed from residual seismic tomography in the upper mantle, *Phys. Earth Planet. Int.*, *99*, 131–143.

Wen, L., and D. L. Anderson (1997b), Present-day plate motion constraint on mantle rheology and convection, *J. Geophys. Res.*, *102*, 24,639–24,653.

Wen, L., and D. L. Anderson (1997c), Layered mantle convection: A model for geoid and topography, *Earth Planet. Sci. Lett.*, *146*, 367–377.

Yoshida, M., and T. Nakakuki (2009), Effects on the long-wavelength geoid anomaly of lateral viscosity variations caused by stiff subducting slabs, weak plate margins and lower mantle rheology, *Phys. Earth Planet. Int.*, *172*, 278–288.

Zhang, S., and U. Christensen (1993), Some effects of lateral viscosity variations on geoid and surface velocities induced by density anomalies in the mantle, *Geophys. J. Int.*, *114*, 531–547.

Zhong, S. (2001), Role of ocean-continent contrast and continental keels on plate motion, net rotation of lithosphere and the geoid, *J. Geophys. Res.*, *106*, 703–712.

Zhong, S., and G. Davies (1999), Effects of plate and slab viscosities on the geoid, *Earth Planet. Sci. Lett.*, *170*, 487–496.

Zhong, S. J., and M. Gurnis (1995a), Mantle convection with plates and mobile, faulted plate margins, *Science*, *267*, 838–843.

Zhong, S. J., and M. Gurnis (1995b), Towards a realistic simulation of plate margins in mantle convection, *Geophys. Res. Lett.*, *22*, 981–984.

Zoback, M. L. (1992), First and second order patterns of stress in the lithosphere: the World Stress Map Project, *J. Geophys. Res.*, *102*, 11,703–11,728.